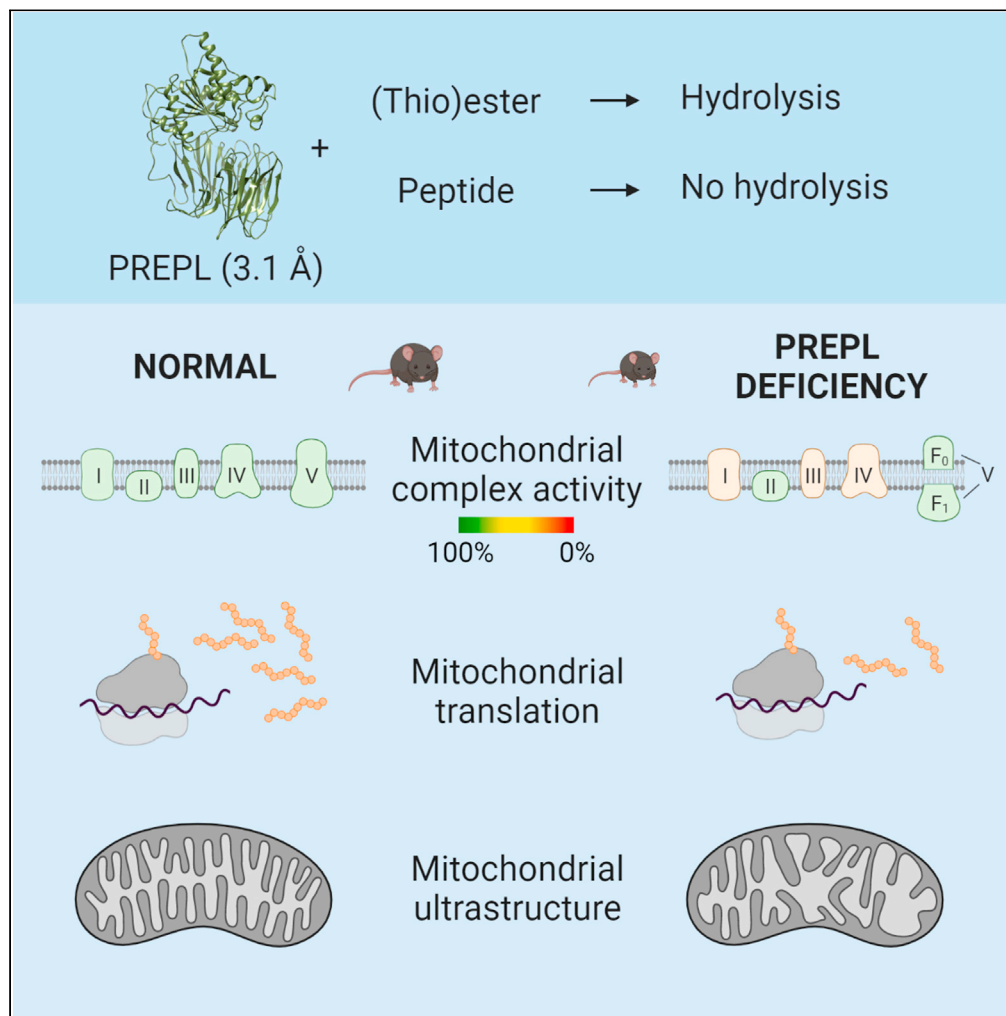**Article**

Prolyl endopeptidase-like is a (thio)esterase involved in mitochondrial respiratory chain function

Karen Rosier, Molly T. McDevitt, Joél Smet, ..., Luc Régal, David J. Pagliarini, John W.M. Creemers

pagliarini@wustl.edu (D.J.P.)
john.creemers@kuleuven.be (J.W.M.C.)

Highlights

Protein interactors connect PREPL with mitochondrial processes

Deficiency of PREPL results in mitochondrial dysfunction in mice (and patients)

Despite homology with peptidases, PREPL has (thio)esterase activity *in vitro*

Crystal structure of PREPL supports the substrate specificity

iScience

Article

Prolyl endopeptidase-like is a (thio)esterase involved in mitochondrial respiratory chain function

Karen Rosier,[1] Molly T. McDevitt,[2] Joél Smet,[3] Brendan J. Floyd,[2] Maxime Verschoore,[3] Maria J. Marcaida,[4] Craig A. Bingman,[2] Irma Lemmens,[5] Matteo Dal Peraro,[4] Jan Tavernier,[5] Benjamin F. Cravatt,[6] Natalia V. Gounko,[7,8] Katlijn Vints,[7,8] Yenthe Monnens,[1] Kritika Bhalla,[1] Laetitia Aerts,[1] Edrees H. Rashan,[2] Arnaud V. Vanlander,[3] Rudy Van Coster,[3] Luc Régal,[1,9] David J. Pagliarini,[2,10,11,*] and John W.M. Creemers[1,12,*]

SUMMARY

Deficiency of the serine hydrolase prolyl endopeptidase-like (PREPL) causes a recessive metabolic disorder characterized by neonatal hypotonia, feeding difficulties, and growth hormone deficiency. The pathophysiology of PREPL deficiency and the physiological substrates of PREPL remain largely unknown. In this study, we connect PREPL with mitochondrial gene expression and oxidative phosphorylation by analyzing its protein interactors. We demonstrate that the long $PREPL_L$ isoform localizes to mitochondria, whereas $PREPL_S$ remains cytosolic. *Prepl* KO mice showed reduced mitochondrial complex activities and disrupted mitochondrial gene expression. Furthermore, mitochondrial ultrastructure was abnormal in a PREPL-deficient patient and *Prepl* KO mice. In addition, we reveal that PREPL has (thio)esterase activity and inhibition of PREPL by Palmostatin M suggests a depalmitoylating function. We subsequently determined the crystal structure of PREPL, thereby providing insight into the mechanism of action. Taken together, PREPL is a (thio)esterase rather than a peptidase and $PREPL_L$ is involved in mitochondrial homeostasis.

INTRODUCTION

Congenital myasthenic syndrome-22 (CMS22, OMIM 616224) is a recessive metabolic disorder caused by mutations in prolyl endopeptidase-like (*PREPL*) (Régal et al., 2014, 2018). PREPL-deficient patients have severe neonatal hypotonia, eyelid ptosis, feeding problems, and growth hormone deficiency. After infancy, the hypotonia remarkably improves and the patients develop hyperphagia and obesity. Most patients have learning difficulties and the average IQ is 70 (Régal et al., 2018). These clinical symptoms are strikingly similar to that of Prader-Willi syndrome (Jaeken et al., 2006). *PREPL* is also involved in several contiguous gene syndromes on chromosome 2p21, such as hypotonia-cystinuria syndrome (HCS), atypical HCS, and 2p21 syndrome, in which one or more flanking genes are additionally deleted (Chabrol et al., 2008; Jaeken et al., 2006; Parvari et al., 2001).

Translation from two alternative start codons gives rise to the 638 amino acids short form, $PREPL_S$, and 727 amino acids long form, $PREPL_L$. Both proteins are identical except for the 89 additional amino acids at the amino-terminus of $PREPL_L$. Both isoforms are catalytically active serine hydrolases, since they react with the activity-based probe (ABP) fluorophosphate-biotin (FP-biotin) (Liu et al., 1999), derived from the serine hydrolase-specific inhibitor diisopropyl fluorophosphate (Jaeken et al., 2006; Szeltner et al., 2005). The serine hydrolase family is a broad family consisting of proteases, lipases, amidases, esterases, and thioesterases (Simon and Cravatt, 2010).

PREPL was provisionally added to the prolyl oligopeptidase subfamily based on sequence similarity and predicted structural homology with prolyl endopeptidase (PREP). PREP is a peptidase cleaving carboxy-terminal of proline residues in peptides smaller than 30 amino acids. The crystal structure of PREP shows an amino-terminal β-propeller domain and a carboxy-terminal catalytic domain formed by an α/β hydrolase fold (Fülöp et al., 1998). Since almost all secondary structure elements are also predicted in PREPL, a similar fold and activity was expected (Jaeken et al., 2006). However, despite multiple different approaches, no peptide substrate could be identified (Martens et al., 2006).

[1]Laboratory for Biochemical Neuroendocrinology, Department of Human Genetics, KU Leuven, Leuven, Belgium

[2]Department of Biochemistry, University of Wisconsin-Madison, Madison, WI 53706, USA

[3]Department of Internal Medicine and Pediatrics, Division of Pediatric Neurology and Metabolism, Ghent University Hospital, Ghent, Belgium

[4]Institute of Bioengineering, School of Life Sciences, Ecole Polytechnique Fédérale de Lausanne (EPFL), Lausanne, Switzerland

[5]Center for Medical Biotechnology, VIB, Department of Biomolecular Medicine, Ghent University, Ghent, Belgium

[6]The Department of Chemistry and The Skaggs Institute for Chemical Biology, The Scripps Research Institute, La Jolla, CA 92037, USA

[7]VIB-KU Leuven Center for Brain & Disease Research, Electron Microscopy Platform & VIB-Bioimaging Core, Leuven, Belgium

[8]Department of Neurosciences, Leuven Brain Institute, KU Leuven, Leuven, Belgium

[9]Department of Pediatrics, Pediatric Neurology and Metabolism, UZ Brussel, Brussels, Belgium

[10]Morgridge Institute for Research, Madison, WI 53715, USA

[11]Departments of Cell Biology and Physiology, Biochemistry and Molecular Biophysics, and Genetics, Washington University

In 2008, PREPL was identified in mouse mitochondria in a mass spectrometry-based proteomics analysis (Pagliarini et al., 2008). Despite the strong evidence for mitochondrial localization, the mitochondrial function of PREPL remains unknown (Floyd et al., 2016). Mitochondrial dysfunction underlies multiple metabolic disorders (Nunnari and Suomalainen, 2012). Interestingly, isolated complex IV as well as combined complex deficiencies have been observed in several PREPL-deficient patients (Bartholdi et al., 2013; Legati et al., 2016; Martens et al., 2007; Régal et al., 2018; Wortmann et al., 2015), suggesting a mitochondrial function of PREPL important for understanding the pathophysiology of CMS22.

In this paper, we report new insights into the function of PREPL as a (thio)esterase and as a mitochondrial protein. We have determined the protein interactors of PREPL to identify pathways and cellular processes in which PREPL is involved. Since a large group of the interactors are mitochondrial proteins, we characterized the connection between PREPL and core aspects of mitochondrial function. We generated *Prepl* KO mice and confirmed mitochondrial dysfunction in this model. In addition, we performed competitive activity-based protein profiling to discover inhibitors of PREPL that pointed to shared features with thioesterases. The results were confirmed using synthetic (thio)ester substrates, and the structural basis of the enzymatic activity was studied using the crystal structure.

RESULTS

Generation and characterization of a *Prepl* KO mouse model

We generated a *Prepl* KO mouse model (Figure S1A) by deleting exon 10, which encodes the catalytic serine residue that has previously been shown to be essential for the hydrolase activity of PREPL (Jaeken et al., 2006). Excision of exon 10 results in a frameshift, causing the loss of the other catalytic triad residues aspartic acid and histidine. No residual protein expression of PREPL or the truncated form, caused by the premature stop codon, was detected in brain of *Prepl* KO mice (Figure 1). Heterozygous mice have an approximately 2-fold reduction in PREPL levels. Non-Mendelian ratios were found after genotyping the offspring of intercrossed heterozygous mice backcrossed once to a C57BL/6 background. Of 394 pups, only 39 (9.9%), instead of the expected 25%, were homozygous *Prepl* KO mice (p < 0.001). The effect is even more pronounced after backcrossing 8 times to a C57BL/6 background (5 homozygous *Prepl* KO mice on 188 pups, or 2.7%, p < 0.001). These backcrossed KO mice die within 1 h after birth due to respiratory failure, consistent with severe respiratory muscle weakness. All subsequent experiments described in this article were therefore performed with 1x backcrossed mice. Weight curves show a lower body weight from birth in *Prepl* KO mice. These KO mice are also significantly smaller than their WT and heterozygous littermates. Body composition of 9-month-old mice was studied using dual-energy X-ray absorptiometry (DEXA) scan (Figure S1B). Bone mineral density was significantly reduced in *Prepl* KO mice. There were no significant differences in the percentage of lean body mass, fat mass, and bone mass relative to total scanned body mass. Taken together, the hypotonia and reduced growth in *Prepl* KO mice resembles the phenotype of patients with CMS22. Differences are the absence of obesity and the prenatal onset of growth restriction.

Protein interactors of PREPL suggest a mitochondrial function for PREPL

Protein interaction partners of PREPL were identified by MAmmalian Protein-Protein Interaction Trap (MAPPIT) (Table S1). This resulted in the identification of 250 interactors. Taking into account previously reported interactors of PREPL collected in the BioGRID database (Stark et al., 2006), the total increased to 285. Functional annotation and enrichment analysis of the interactors was performed using g:Profiler (Raudvere et al., 2019). A significant enrichment was found for mitochondria (75 interactors (30.1%), p = 3.095E-20) and mitochondrial gene expression (p = 2.51E-10). Nine of the mitochondrial proteins play a role in oxidative phosphorylation and 18, mostly subunits of the mitoribosomes, are involved in mitochondrial translation (p = 8.532E-10; Figure 2A; Table S2). We determined the cellular localization of endogenous PREPL in HEK293T cells (Figure 2B). We did indeed detect PREPL in the mitochondria, labeled with Mitotracker, although PREPL staining is clearly not restricted to the mitochondria. Consistently, PREPL was detected both in the cytosolic and mitochondrial fractions of HEK293T cells.

PREPL$_L$ is translocated into the mitochondria

No mitochondrial targeting sequence (MTS) is predicted for the human long or short isoform of PREPL (Figure 2C; Table S3). In contrast, an MTS is predicted in murine PREPL$_L$. After translocation into the mitochondrial matrix, mitochondrial processing peptidase (MPP) cleaves off the MTS of most mitochondrial proteins.

School of Medicine, St Louis, MO 63110, USA

[12]Lead contact

*Correspondence:
pagliarini@wustl.edu (D.J.P.),
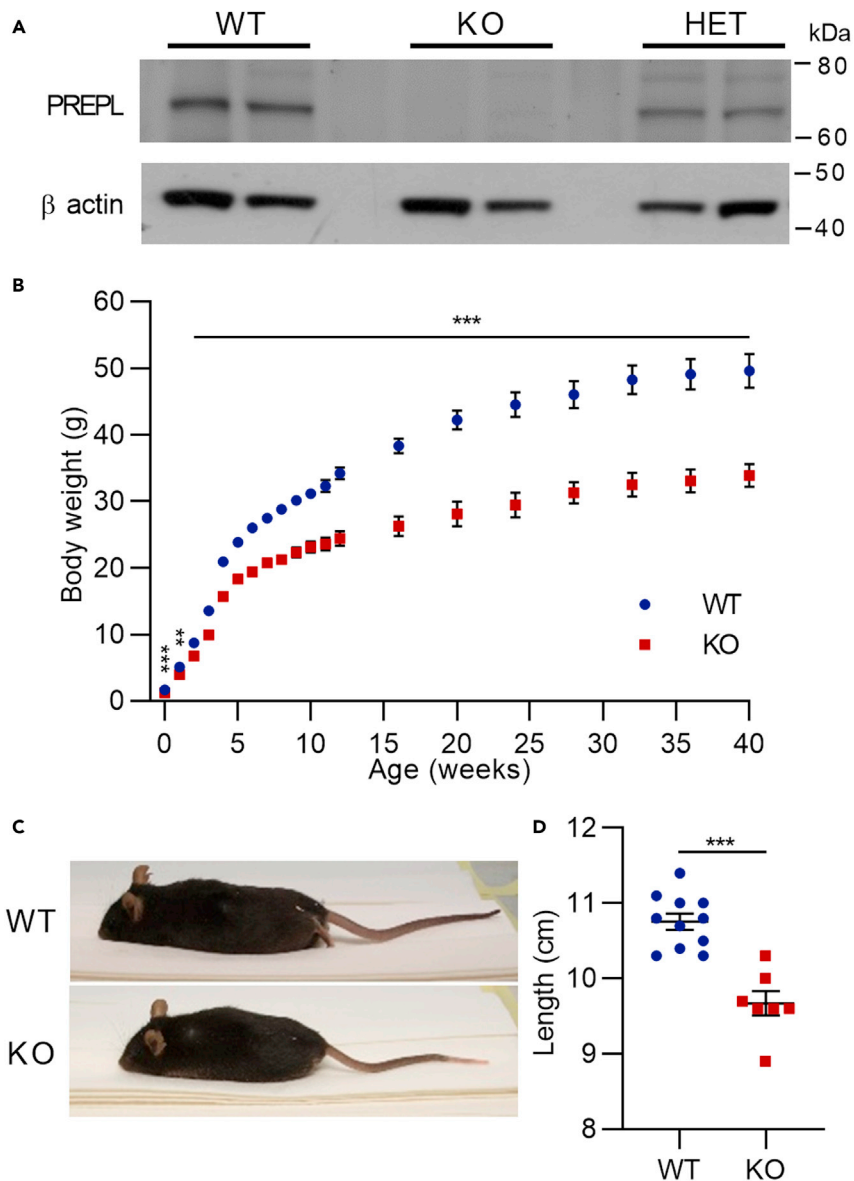john.creemers@kuleuven.be
(J.W.M.C.)

Figure 1. *Prepl* KO mice show a partial phenocopy of patients with CMS22

(A) Western blot analysis confirms the absence of PREPL expression in brain of *Prepl* KO mice. Intermediate expression levels are seen in heterozygous mice.

(B) Weight curves of male *Prepl* WT and KO mice (n = 8–11) show that KO mice weigh less than WT mice from birth.

(C) *Prepl* KO mice are smaller than WT mice. Representative example of body size difference of WT and KO male mice at 9 months.

(D) Length measurement in 9-month-old male mice reveals significant differences in length of *Prepl* WT and KO mice (n = 7–11). (B–D) Data are shown as mean $\pm$ SEM; unpaired Student's t test; **p < 0.01; ***p < 0.001.

See also Figure S1.

MitoFates detected a possible cleavage site for MPP at amino acid position 69 of human PREPL$_L$. In addition, a cleavage site for the intermediate cleavage peptidase Icp55 is predicted at position 70. Icp55 is known to cleave single amino acids after MPP processing to obtain a stable, mature, and functional protein (Poveda-Huertes et al., 2017). Cleaving off the 70 amino-terminal amino acids of human PREPL$_L$ would result in a 657-amino-acid protein with a molecular weight of ~75 kDa, 2 kDa more than PREPL$_S$ (638 amino acids). This is significantly less than the calculated 10-kDa difference between full-length PREPL$_L$ (727 amino acids) and PREPL$_S$. The 2-kDa difference in molecular weight was indeed observed between the cytosolic
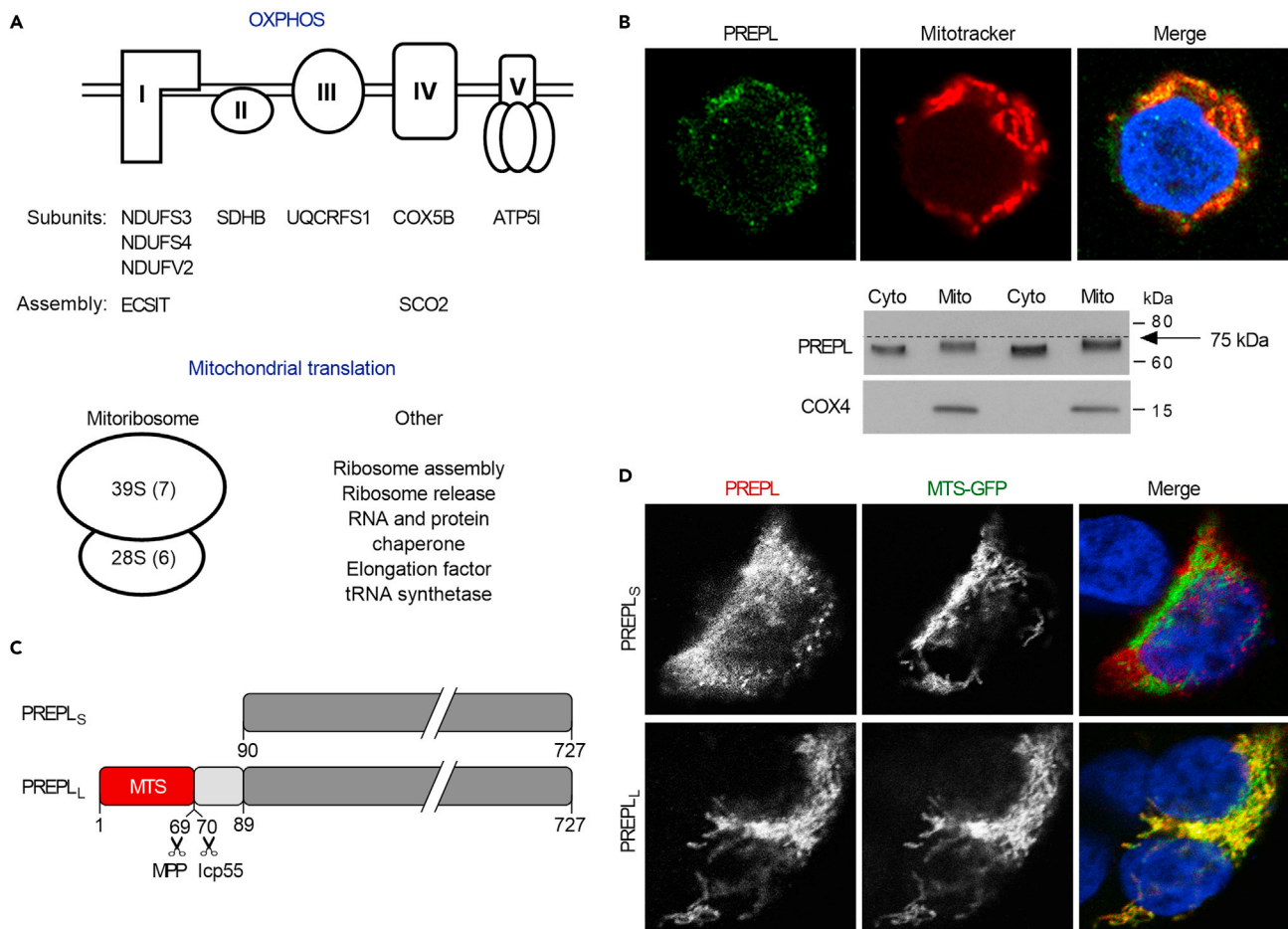
Figure 2. PREPL$_L$ is translocated into the mitochondria

(A) Thirty percent of the interaction partners of PREPL are linked to mitochondria, with interactors related to oxidative phosphorylation (OXPHOS) and mitochondrial translation. The number of PREPL protein interactors related to the large (39S) or small (28S) subunit of the mitoribosome is indicated between brackets. See also Tables S1 and S2.

(B) Co-staining of endogenous PREPL (green) with Mitotracker (red) in HEK293T cells. DAPI (blue) was used for nuclear counterstaining. Endogenous PREPL is found in the cytosolic and mitochondrial fractions of HEK293T cells. An ∼2-kDa difference is observed for cytosolic and mitochondrial PREPL. Dashed line is the reference for the molecular weight of the mitochondrial form. COX4 is used as a mitochondrial marker.

(C) Schematic representation of the predicted mitochondrial targeting signal (MTS, red). Predicted cleavage sites of MPP and Icp55 in PREPL$_L$ are highlighted. See also Table S3.

(D) Colocalization of PREPL$_L$ (red) with MTS-GFP (green).

and mitochondrial form of PREPL in HEK293T (Figure 2B). To substantiate this finding, we compared the localization of recombinant PREPL$_S$ and PREPL$_L$ in HEK293T cells with that of GFP fused to an amino-terminal MTS (MTS-GFP) (Figure 2D). Extensive colocalization was found for PREPL$_L$ but not for PREPL$_S$, confirming that PREPL$_L$ contains an MTS that targets this isoform to the mitochondria.

Loss of PREPL causes respiratory chain defects

To examine the role of PREPL$_L$ in mitochondrial function, we measured the activity of the mitochondrial respiratory chain complexes in quadriceps of *Prepl* KO mice (Figure 3). Activities of individual complexes are normalized to citrate synthase as measure for mitochondrial content. Activity was reduced for complex I and IV (30%) and for complex III (60%), all complexes containing mtDNA-encoded subunits. Since expression of PREPL is highest in the brain, the respiratory chain activity was also measured in the cortex and cerebellum. A reduction of the activity of complexes I, III, and IV was observed here as well. In the cortex, a 30% increase of complex II was seen. Because of deficiencies in complexes containing mtDNA-encoded subunits, we speculated that complex V activity would also be impaired. We used blue native polyacrylamide
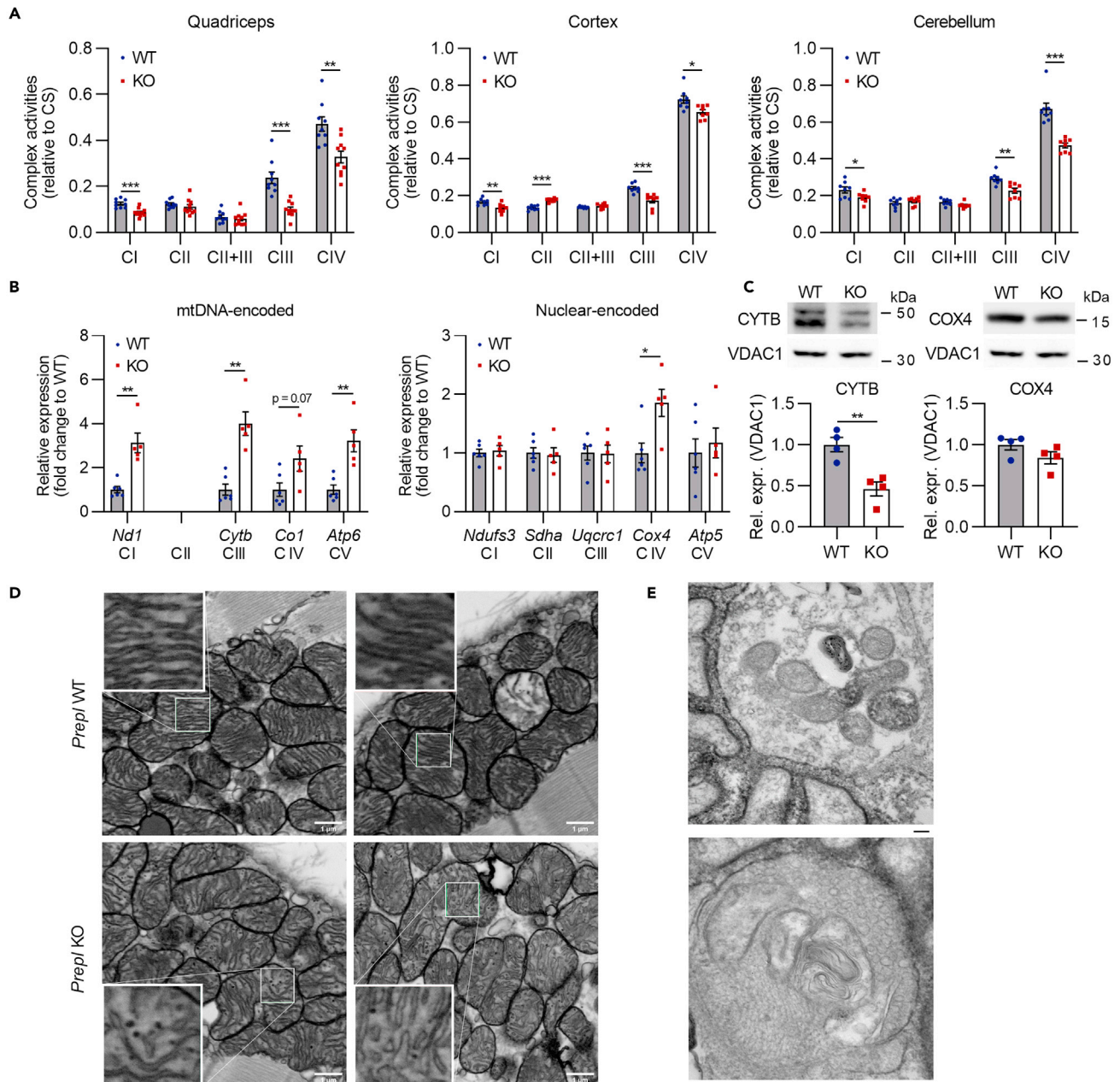
Figure 3. PREPL deficiency results in mitochondrial dysfunction

(A) Activity of complexes I, III, and IV is decreased in quadriceps, cortex, and cerebellum of *Prepl* KO mice. Complex activities are normalized to citrate synthase (CS; n = 6–10, 12-week-old male mice).

(B) RT-qPCR reveals enhanced transcription of mtDNA-encoded complex subunits in quadriceps (n = 5–6; 12-week-old male mice). β-Actin was used as a housekeeping gene.

(C) Expression of CYTB and COX4 in mitochondrial fractions of *Prepl* KO quadriceps (n = 4). VDAC1 is used for normalization. A-C. Data are represented as mean ± SEM; Unpaired Student's t test; *p < 0.05, **p < 0.01, ***p < 0.001.

(D) Mitochondria in skeletal muscle of WT and *Prepl* KO mice. Scale bars represent 1 μm. Cristae are structured and densely packed in WT mice. Mitochondria in *Prepl* KO mice contain swollen or broken cristae and have more space between the cristae. Representative pictures of two WT and two KO mice.

(E) Abnormal mitochondrial morphology in nerve terminal of a PREPL-deficient patient. Mitochondria appear swollen with loss of cristae and myeloid structures. Some mitochondria are engulfed in autophagosomes. The black reaction product on the junctional folds localizes AChR with peroxidase-labeled α-bungarotoxin (Régal et al., 2014). Scale bars represent 100 nm.

gel electrophoresis (BN-PAGE) to isolate protein complexes from whole tissue homogenates (Van Coster et al., 2001). BN-PAGE followed by in-gel activity staining confirmed the previously described complex deficiencies (Figure S2). The amounts of complex V holoenzyme are comparable between WT and KO mice, suggesting limited differences in complex V activity. However, a complex V subcomplex was consistently observed in quadriceps of *Prepl* KO mice. The mtDNA-encoded subunits of complex V are necessary to connect the intramembrane (F_0) and ATPase (F_1) domain of complex V. A reduced number of these mtDNA-encoded subunits, caused by defective mitochondrial translation, can result in complex V assembly problems with dissociation of the ATPase domain (Smet et al., 2009). Of notice, the presence of complex V subcomplexes are sometimes observed in samples with high mitochondrial activity or as a consequence of compromised sample preparation.

Mitochondrial protein synthesis is decreased in quadriceps of *Prepl* KO mice despite increased transcription

To study the effect of PREPL deficiency on mitochondrial gene expression, we first measured the steady-state levels of nuclear DNA and mitochondrial DNA (mtDNA)-encoded mRNAs by RT-qPCR in quadriceps of *Prepl* KO mice (Figure 3B). Expression of mtDNA-encoded subunits of complexes I, III, and V was enhanced. Expression of nuclear-encoded subunits was similar in both groups except for *Cox4*, a subunit of complex IV, which was also increased in the KO mice. Increased mitochondrial transcription levels are often found in mouse models with impaired mitochondrial protein synthesis, as a potential compensatory mechanism for respiratory chain defects (Cámara et al., 2011; Szczepanowska et al., 2016). Consistently, we found decreased protein levels of the mtDNA-encoded cytochrome *b* (CYTB) in quadriceps of *Prepl* KO mice, whereas protein levels of the nuclear-encoded COX4 were not significantly altered (Figure 3C).

Structural abnormalities of mitochondria in *Prepl* KO mice and a PREPL-deficient patient

Ultrastructural analysis revealed altered mitochondrial morphology in quadriceps of *Prepl* KO mice (Figure 3D). Mitochondria of WT mice contain densely packed parallel cristae, whereas the mitochondrial matrix in *Prepl* KO mice is less densely packed and cristae are more randomly distributed. Furthermore, dilated and broken cristae can be observed. Previously, we studied the ultrastructure of the neuromuscular junction in a PREPL-deficient patient (Régal et al., 2014). Re-evaluation of these electron micrographs revealed abnormal morphology in 5 of the 56 mitochondria (∼9%) of the PREPL-deficient patient (Figure 3E), whereas control samples usually have <1% abnormal mitochondria. Mitochondria at the nerve terminal appeared swollen with loss of cristae. In addition, we observed mitophagy, which occurs as a consequence of mitochondrial swelling.

Palmostatin M inhibits PREPL

We performed competitive activity-based protein profiling (ABPP) to screen an inhibitor library with inhibitors targeting specific subfamilies of the serine hydrolase family (Figures 4 and S3 and Table S4). Only two inhibitors inhibited the interaction between FP-biotin and PREPL by at least 50%. Palmostatin M decreased the catalytic activity of PREPL by ∼90%, comparable with inhibitor 8 (1-isobutyl-3-oxo-3,5,6,7-tetrahydro-2H-cyclopenta[c]pyridine-4-carbonitrile), a known inhibitor of PREPL (Lone et al., 2012). The reaction between PREPL and FP-biotin was reduced to 49% when incubated with WHP313, a broad-spectrum serine hydrolase inhibitor (Figure S3A). Palmostatin B, which is structurally related to Palmostatin M, was not able to inhibit PREPL (Figure 4B). Palmostatin M is a known inhibitor of acyl protein thioesterase 1 and 2 (APT1 and APT2). We also tested the serine hydrolase inhibitors on PREP, the closest human paralog of PREPL, in an assay with z-Gly-Pro-AMC as substrate (Figure S3B) (Bracke et al., 2019). In contrast to PREPL, the activity of PREP was not inhibited after incubation with Palmostatin M.

PREPL has *in vitro* (thio)esterase activity

The results of the inhibitor studies revealed inactivation of PREPL activity by an acyl protein thioesterase inhibitor. Therefore, we investigated whether bacterially expressed PREPL harbors thioesterase activity (Figure 4C). PREPL was as active as APT1 in hydrolyzing the short-chain thioester substrate NPTA. Since most thioesterases also cleave ester substrates, we subsequently used chromogenic ester substrates of different chain lengths to assess the esterase activity and substrate specificity of PREPL (Figure 4D). The results indicate that PREPL indeed has esterase activity and is able to cleave short-chain p-nitrophenyl ester substrates. Esterase activity was not observed with the catalytically inactive serine mutant of PREPL. The activities of both PREPL and APT1 toward the ester substrates decrease as the length of the side chain increases, perhaps due to the absence of a lipid bilayer in this *in vitro* assay. The Michaelis-Menten kinetic
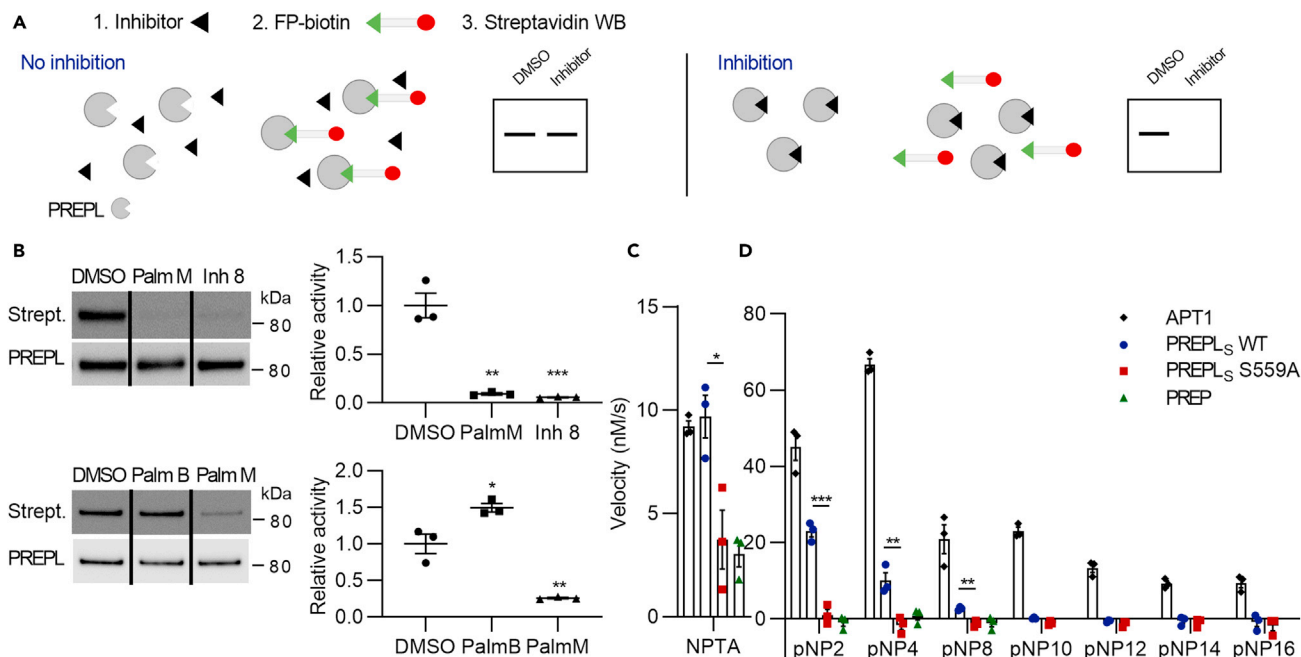
Figure 4. PREPL is inhibited by acyl protein thioesterase inhibitor Palmostatin M and has (thio)esterase activity *in vitro*

(A) Principle of competitive ABPP. The activity-based probe FP-biotin is able to react with catalytically active PREPL. This interaction can be detected by streptavidin blotting. In the presence of an active PREPL inhibitor, FP-biotin is not able to label PREPL.

(B) Palmostatin M inhibits PREPL to the same extent as inhibitor 8 (1-isobutyl-3-oxo-3,5,6,7-tetrahydro-2H-cyclopenta[c]pyridine-4-carbonitrile), a known inhibitor of PREPL. Streptavidin-labeled blot shows the interaction of PREPL with FP-biotin. The amount of GST-tagged PREPL present is determined with a GST antibody. Lanes run on same gel but are noncontiguous. Data are shown as mean $\pm$ SEM (n = 3). Differences with DMSO control were analyzed by one-way ANOVA with Dunnett's multiple comparison test. See also Figure S2.

(C) PREPL cleaves the thioester substrate p-nitrophenyl thioacetate (NPTA) as efficient as APT1. Importantly, residual thioesterase activity is still observed for the PREPL S559A mutant and PREP.

(D) Activity of PREPL and the inactive serine mutant PREPL S559A on p-nitrophenyl (pNP) acetate (pNP2), butyrate (pNP4), octanoate (pNP8), decanoate (pNP10), dodecanoate (pNP12), myristate (pNP14), and palmitate (pNP16). PREP is not able to hydrolyze the ester bonds. Unpaired Student's t test was performed between WT and PREPL S559A. C-D. Data are represented as the blank-corrected velocity. Data are shown as mean $\pm$ SEM (n = 3); *p < 0.05, **p < 0.01, ***p < 0.001.

parameters were determined for the short-chain esters (pNP2 and pNP4) and thioester substrates (Table 1). The catalytic efficiency of PREPL for pNP2 was similar with published values for human APT (0.26 and 0.12 $s^{-1} \cdot mM^{-1}$ for PREPL and human APT1, respectively) (Filippova et al., 2013). However, the efficiency of pNP4 hydrolysis was found to be considerably lower for PREPL (0.14 and 3.1 $s^{-1} \cdot mM^{-1}$ for PREPL and human APT1, respectively). NPTA hydrolysis is more efficient compared with the ester substrates, which can be expected since thiolates are better leaving groups. PREP was not able to hydrolyze any of the short-chain ester substrates, while limited thioester hydrolysis was observed.

Structure of PREPL$_S$

In order to rationalize the newly discovered (thio)esterase activity of PREPL, the crystal structure of human PREPL$_S$ was solved at 3.1-Å resolution. The crystals belong to the I222 space group with one PREPL$_S$ molecule in the asymmetric unit. Despite the relatively low resolution of the data, the model contains 624 of the 638 amino acids, the missing residues being in the flexible amino- and carboxy-termini (Figure 5; Table S5).

As expected, PREPL has the same architecture as other members of the family, i.e., a cylindrical shape, ~75 Å high and ~50 Å in diameter (Figure 5A). It is composed of two domains: the amino-terminal seven-bladed β-propeller domain, each blade with four antiparallel β-strands, and the carboxy-terminal catalytic domain with an α/β hydrolase fold. Residues 424–440 form a hinge loop that connects the two domains. The active site, with the catalytic triad residues S559, D645, and H690, is at the interface of the two domains (Figure 5B). Our crystal structure shows PREPL$_S$ in an inactive conformation, similar to that observed in structures of other prolyl oligopeptidase family members, such as PREP (Li et al., 2010; Shan et al., 2005), Oligopeptidase B

Table 1. Kinetic parameters of (thio)esterase activity

	V_{max} ($\mu M \cdot s^{-1}$)	k_{cat} (s^{-1})	K_M (mM)	k_{cat}/K_M ($s^{-1} \cdot mM^{-1}$)
pNP2	0.025	0.11	0.43	0.26
pNP4	0.014	0.06	0.42	0.14
NPTA	0.072	0.30	0.49	0.61

(OpdB) (Canning et al., 2013), and acylaminoacyl peptidase (AAP) (Harmat et al., 2011; Kiss et al., 2007; Wang et al., 2006). The root-mean-square deviation (RMSD) values between our inactive form of human PREPL$_S$ and the inactive structures of PREP (PDB 3IUL), OpdB (PDB 4BP8), and AAP (PDB 3O4G) are 4.2, 3.5, and 4.5 Å, respectively (Figures S4 and S5). This conformation is characterized by a large interdomain opening (Figures 5A and S5) and a rearrangement of the His-loop, an ~10-amino-acid flexible loop that contains the catalytic H690. Hydrogen/deuterium exchange mass spectrometry has shown that the His-loop in human PREP is flexible in the absence of a ligand/inhibitor and becomes more rigid in the presence of ligand/inhibitor (Tsirigotaki et al., 2017). In the PREPL$_S$ inactive form, H690 swings out toward the surface, ~20 Å from the active form position, and is stabilized by Q155 and E177 from the β-propeller domain (Figures 5B and S5C).

Two major differences between PREPL$_S$ and the other three enzymes can be observed in the first amino-terminal residues and in the first blade of the β-propeller (red in Figure 5 and red/orange in Figure S5). In PREP and in OpdB, the amino-terminal residues 7–71 wrap around the α/β hydrolase fold encoded by the carboxy terminus, together forming the catalytic domain. In AAP, residues 7–22 form an α-helix that packs against the catalytic domain. Conversely, in PREPL$_S$ the amino terminus (residues 90–111) is buried in the interface. The signal from the Se-methionine anomalous difference map allowed us to unambiguously place M90. We could build the following ten residues forming a helix inside the cavity, resembling the helix insertion in a loop in the fourth blade of the β-propeller in dipeptidylpeptidase IV (DPP4) that also belongs to the prolyl oligopeptidase family (Figures S6) (Aertgeerts, 2004). The conformation of the amino terminus of PREPL inside the cavity has not been observed before and may have important implications for PREPL activity, as discussed below.

In the PREPL$_S$ inactive conformation, the β-propeller domain defines a funnel shape with dimensions of ~25 Å diameter at the top aperture and ~12 Å at the bottom aperture. The first blade of the β-propeller is displaced downward away from the His-loop and far away from the last blade (blade 7), opening the circle by ~12 Å and creating a side entrance to the funnel (Figure S6). The conformation of the first blade differs from that in the inactive forms of PREP, OpdB, and AAP, where blades 1 and 7 are closer to each other (~8 Å).

The structure of the carboxy-terminal catalytic domain is comparable with that of the canonical α/β hydrolase fold and superimposes well with the catalytic domains of PREP, OpdB, and AAP (RMSD = 1.0, 0.8, and 4.6 Å, respectively, Figure S7A). Previous crystal structures of enzyme-ligand complexes revealed that the peptide-binding pockets in PREP, OpdB, AAP, and DPP4 (i.e., PDB ID 3DDU, 4BP9, 2HU5, and 1R9N) form at the interface, by domain closure, involving residues from the two domains. Comparing PREPL$_S$ to the inhibitor-bound OpdB closed structure (Figures 5C and S7B), it seems that the amino terminus of PREPL$_S$ would clash with the docked ligand, as it occupies part of the equivalent putative peptide-binding pocket. The amino terminus, however, does not interfere with the rearrangement of the His-loop into a catalytically active form, as PREPL$_S$ reacts with FP-biotin. Interestingly, the residues that form the peptide-binding site in *Trypanosoma brucei* Opdb (PDB ID 4BP9) described in Canning et al. (2013) are all conserved in PREPL$_S$ except E655 (E624 in *E. coli* OpdB), which in PREPL$_S$ is G652 (Figure S7C), and the equivalent residues in the β-propeller domain, E172, K208, and D214. In OpdB, E655 recognizes the P1 arginine residue (Canning et al., 2013). In AAP and PREP, this position is occupied by a proline and a histidine, respectively, highlighting the different substrate specificities of the enzymes (Figure S4). Conversion of the glutamic acid to a glycine in *E. coli* OpdB (OpdB E624G) resulted in an approximately 2-fold decrease of its peptidase activity (Figure S7D). Creating the opposite mutation in PREPL (G652E), thereby mimicking the peptide-binding site of OpdB, did not result in peptidase activity of PREPL.

Since PREPL$_S$ has (thio)esterase activity, we investigated a possible lipid-binding site in our crystal structure. We compared PREPL$_S$ with other esterases with an α/β hydrolase fold that structurally align with low RMSD values (<5 Å) and that have been crystallized with substrates or inhibitors, like APT1 (PDB ID 6QGN [Abrami et al., 2021]), monoacylglycerol lipase (PDB ID 6AX1), and the archaeal AAP (PDB ID 3O4G), that have both peptidase and esterase activity. The structure comparison guided the docking experiments that revealed a putative lipid-binding pocket, as seen for pNP8 in Figure 5D. This pocket partly overlaps with the hydrophobic part of the
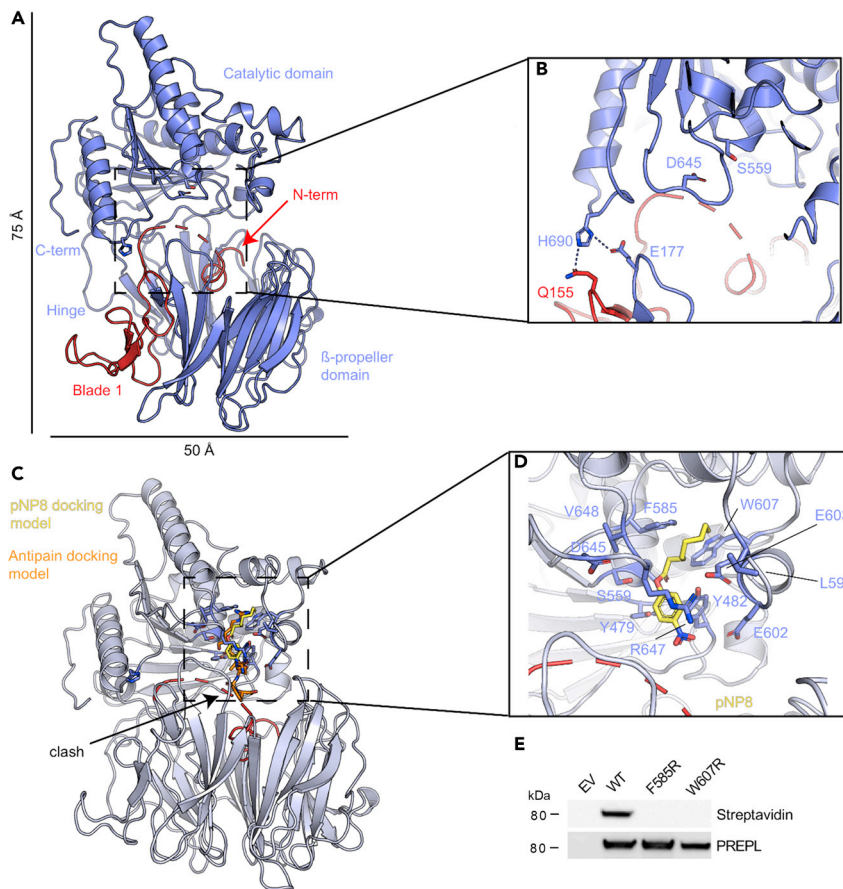
Figure 5. Crystal structure of human PREPL$_S$ contains a putative lipid-binding pocket

(A) Cartoon representation of PREPL$_S$ in blue with the amino terminus and the first blade of the β-propeller (blade 1) highlighted in red. The catalytic domain containing an α/β hydrolase fold is shown on top of the β-propeller domain. The amino- and carboxy-termini are indicated, as well as the hinge region that connects the two domains.

(B) The catalytic triad residues S559, D645, and H690 are found at the interface between the two domains. The displaced H690 interacts (dashed lines) with Q155 and E177 from the β-propeller domain.

(C) Modeling of ligand binding into the PREPL$_S$ structure. Antipain, the ligand covalently bound to OpdB in PDB ID 4BP9, is shown as orange sticks into the equivalent position in PREPL$_S$, where it clashes with the amino terminus of PREPL$_S$ in red. pNP8, shown as yellow sticks, is modeled bound to the proposed putative lipid-binding pocket.

(D) Detailed view of the putative lipid-binding pocket, with PREPL$_S$ residues shown as blue sticks and pNP8 shown as yellow sticks.

(E) The mutations of residues that form part of the putative lipid-binding pocket F585R and W607R render PREPL$_S$ inactive in the FP-biotin activity assay.

peptide-binding pocket present in other prolyl oligopeptidase family members but does not extend to the β-propeller domain. The potential binding pocket is formed by R647, Y479, Y482, and E602, close to the catalytic S559, as well as E603, W607, F585, V648, and L599. Mutating F585 and W607, two hydrophobic residues that line up the pocket, to arginine, with a large and positive side chain, resulted in inactive PREPL in the FP-biotin assay (Figure 5E), supporting their role in forming an active site conformation compatible with catalysis.

DISCUSSION

In this study, we have unveiled a role for PREPL in mitochondrial complex activity and gene expression. Furthermore, we have demonstrated that PREPL has (thio)esterase rather than peptidase activity, and we found indications that PREPL might be a depalmitoylase. We describe, for the first time, the crystal structure of PREPL$_S$.

The *Prepl* KO mice generated for this study have impaired growth and background-dependent neonatal hypotonia, similar to the phenotype of patients with CMS22 and the previously described PREPL null

mice (Lone et al., 2014). In the latter, neonatal hypotonia was demonstrated by surface-righting and grip strength assay, however, using pups of mixed backgrounds (C57BL/6 and SW). The grip strength assays at adult age revealed no differences between control and KO mice, suggesting that hypotonia improves over time as observed in affected patients. In our model, decreased bone mineral density was also observed, which may be related to growth hormone deficiency or hypotonia (Butler et al., 2001; Capozzi et al., 2013). However, although the impaired growth seems to recapitulate the human phenotype of growth hormone deficiency, the *Prepl* KO mice were smaller from birth. This indicates deficient prenatal growth, which is not growth hormone dependent (Randhawa and Cohen, 2005).

Although we initially showed that PREPL is present in the cytoplasm (Jaeken et al., 2006), interacting with the cytoskeleton and the *trans-Golgi network* (Morawski et al., 2013; Radhakrishnan et al., 2013), proteomics analysis of isolated mitochondria have revealed that PREPL is also present in the matrix of mitochondria (Pagliarini et al., 2008; Rhee et al., 2013). Here we show that only the PREPL$_L$ isoform is translocated into the mitochondria, while the short isoform remains cytosolic. Mitochondrial complex activity measurements showed reduced complex I, III, and IV activity in skeletal muscle and brain of *Prepl* KO mice. This pattern of combined complex deficiency, with sparing of complex II, the only mitochondrial complex independent of mtDNA expression, points toward a faulty mitochondrial transcription or translation (Mayr et al., 2015). This is consistent with the finding that several PREPL interactors have key roles in these mitochondrial processes. An increased complex II activity was observed in the cortex. This probably reflects a compensatory increase in nuclear-encoded mitochondrial proteins, a situation often observed when deficient mitochondrial transcription or translation is present. In addition, a complex V subcomplex was observed in the *Prepl* KO mice, pointing toward assembly problems caused by defective mitochondrial translation (Smet et al., 2009). Moreover, our study shows a decrease in the protein levels of the mtDNA-encoded CYTB and an increase in steady-state levels of mtDNA-encoded transcripts, whereas nuclear-encoded subunits remained unchanged in *Prepl* KO mice. The upregulation of mtDNA-encoded transcripts is likely a compensatory mechanism for impaired translation, as has been observed in other mouse models with reduced mitochondrial translation such as *Clpp* and *Mterf4* KO mice (Cámara et al., 2011; Szczepanowska et al., 2016). Mitochondria of *Prepl* KO mice are less densely packed with cristae that are frequently broken or swollen. Cristae shape varies within different tissues; however, cristae form and function are closely linked, as they provide the framework for mitochondrial complexes (Pánek et al., 2020). Upon inhibition of mitochondrial translation, cristae have been observed as short stubby tubules in fibroblast (Richter et al., 2013). It is currently unknown how PREPL deficiency affects the shape and distribution of the cristae. Many players are involved in these processes, including cardiolipin, ATP synthase dimers, Opa1, and the MICOS complex. After *de novo* synthesis of the phospholipid cardiolipin in the mitochondrial matrix, acyl chain modifications are required to produce mature cardiolipin (Ye et al., 2016). CLD1p is the only specific cardiolipin deacylase in yeast; the mammalian homolog is not yet identified.

The observation of mitochondrial dysfunction in *Prepl* KO mice is in line with the decreased complex activities observed in some patients with HCS and CMS22 (Bartholdi et al., 2013; Legati et al., 2016; Martens et al., 2007; Régal et al., 2018; Wortmann et al., 2015). Also, swollen mitochondria with loss of cristae in the nerve terminal of a PREPL-deficient patient further supports the presence of mitochondrial dysfunction in PREPL-deficient patients. Primary mitochondrial disorders are often multi-systemic, mainly affecting tissues with high energy demands such as brain and skeletal muscle (Kanungo et al., 2018). PREPL is ubiquitously expressed, with the highest expression levels found in brain; intermediate levels in heart, skeletal muscle, kidney, and neuroendocrine cells; and low levels in all other tissues tested (Jaeken et al., 2006). Patients affected with mitochondrial diseases present symptoms such as hypotonia, failure to thrive, growth restriction, and cognitive problems, all of which are seen in patients with CMS22. However, it is difficult to assess the clinical relevance of the relatively mild decreases of mitochondrial complex activities we found. The upper limit of residual mitochondrial complex activities to support diagnosis of a primary mitochondrial disorder traditionally is set at 20%–40% of normal, lower than what we observed. Neuromuscular junction abnormalities have been reported to occur in about 25% of patients with mitochondrial diseases (Braz et al., 2019). However, as micro-electrode studies of the neuromuscular junction typically are not performed in patients with mitochondrial disorders, it is unclear if the decreased quantal content of the endplate potential and reduced amplitude of the miniature endplate potential that were found in a PREPL-deficient patient also occur in mitochondrial disease (Régal et al., 2014). Mutations of the mitochondrial citrate carrier *SLC25A1* cause a rare example of a well-defined congenital myasthenic syndrome associated with mitochondrial dysfunction, but quantal content and miniature endplate potential were normal in this disorder (Chaouch et al., 2014). As PREPL$_S$ remains cytosolic, the cytosolic deficiency of PREPL most probably is

responsible for at least part of the phenotype. In the cytoplasm, PREPL binds the µ1A subunit of the clathrin-associated adaptor protein complex 1 (AP-1). It reduces membrane binding of AP-1, which mediates the formation of clathrin-coated vesicles for transport and secretion (Radhakrishnan et al., 2013). Although we could link the previously uncharacterized mitochondrial protein with mitochondrial gene expression and respiratory chain function, it is presently unclear how PREPL impacts these cellular processes, as the physiological mitochondrial substrates remain to be identified.

Serine hydrolases consist not only of peptidases like the closest human PREPL homolog PREP but also esterases and lipases (Bisogno et al., 2003; Quinn, 1987; Stafforini et al., 1987). AAP, one of the prolyl oligopeptidase (S9) family members, exhibits both esterase and peptidase activities (Bartlam et al., 2004; Wang et al., 2006). A competitive ABPP screen using inhibitors against specific subclasses of serine hydrolases showed that Palmostatin M, an inhibitor of APT1 and APT2, is also able to inhibit PREPL. This is in accordance to structural motifs present in PREPL, like the HxxxD motif near the active site histidine that is highly conserved in acyltransferases. In addition, PREPL contains an AxSxG motif surrounding the catalytic serine. This motif is also found in multiple esterases and lipases, such as CLD1p (Baile et al., 2013) and PLA2G15 (Shayman and Tesmer, 2019), but not in peptidases. Finally, we demonstrated that PREPL is able to cleave synthetic (thio)ester substrates *in vitro*, thereby definitively attributing the first catalytic activity to PREPL.

We describe the first crystal structure of a mammalian member of the prolyl oligopeptidase family in an open conformation. So far, all mammalian PREP proteins, even in the apo state, have been crystallized in the closed state. Obtaining this open structure of human PREPL$_S$ supports the idea that across the S9 family in all domains of life, in the free form, these enzymes exist in a conformationally flexible open state, as suggested by (Li et al., 2010) and (Canning et al., 2013).

The structural and biochemical analyses presented highlight the close similarity between PREPL and other members of the family, in particular OpdB, and prove that the underlying mechanisms dictating substrate specificity are not straightforward. On the one hand, using the PREPL G652E mutant, which mimics the OpdB peptide-binding pocket at the α/β hydrolase domain (Figure S6), we have shown that the differences in the conformation of the amino terminus and of the β-propeller domain or in the dynamics of domain closure must be responsible for the lack of peptidase activity of PREPL. On the other hand, structural comparisons with other esterases bound to ligands and molecular docking experiments have led us to propose a putative lipid-binding pocket located exclusively within the α/β hydrolase domain. The peptide-binding pocket in OpdB and PREP is formed by residues from both domains, and domain closure is needed to form the pocket and align peptide substrates for hydrolysis. We propose that PREPL$_S$ is unable to cleave peptides because the conformation of the amino terminus prevents peptide binding and domain closure. In this model, the amino terminus is auto-inhibitory for peptidase activity. Nonetheless, PREPL$_S$ is able to bind and cleave lipids, as the amino terminus does not interfere with the lipid-binding pocket and the formation of an active catalytic triad. It is unclear whether the observed position of the amino terminus, which may be flexible, is a crystallization artifact or an auto-inhibitory mechanism present at all times. In AAP and DPP4, the amino terminus that packs against the catalytic domain is shorter than that of PREP or OpdB but still forms a helix that packs against the catalytic domain (orange in Figures S4 and S5). This surface is already occupied by the carboxy-terminal end (residues 712–720) of PREPL$_S$, suggesting that the amino terminus in PREPL$_S$ cannot adopt the conformation seen in the other enzymes and therefore adopts a conformation that is incompatible with the formation of a peptide-binding pocket. In addition, stabilization of the closed state by the β-propeller domain, which is required for the alignment of the peptide substrate, is not supported by the downward conformation of the first blade of the β-propeller.

This structural analysis provides insight into the newly discovered esterase activity of PREPL. The putative lipid-binding pocket superimposes with the hydrophobic region of the peptide-binding pocket found in OpdB and other family members. As a result, many of the residues that line the pocket are conserved. It is, however, still not clear which residues determine specificity and whether the β-propeller domain is required for esterase activity. Further structure-function studies will be required to elucidate the identification and recognition mode of esterase substrates.

Multiple esterases and thioesterases are known to act within mitochondria. For example, ICT1 is a peptide-tRNA hydrolase, which cleaves the ester bond between amino acids and tRNA in prematurely terminated polypeptides, thereby recycling stalled mitoribosomes. Also, acyl-CoA thioesterases, which catalyze the hydrolysis of coenzyme A (CoA) esters to free fatty acids and CoA, are known to regulate β-oxidation and intracellular levels of

CoA esters, free fatty acids, and CoA in mitochondria. We showed that PREPL is inhibited by the depalmitoylase inhibitor Palmostatin M. Consistent with this, it was reported that PREPL is inhibited 50% by hexadecyl fluorophosphonate, a probe designed to specifically identify depalmitoylating enzymes of the serine hydrolase family (Lin and Conibear, 2015; Martin et al., 2012). APT1 is a cytosolic enzyme, known to depalmitoylate H-Ras, SNAP23, and the alpha subunit of G proteins (Zeidman et al., 2009). However, using a mitochondria-specific fluorescent depalmitoylating probe, APT1 was found to be an active, mitochondrial depalmitoylase (Kathayat et al., 2017). Treatment of three different cell types with Palmostatin B, a broad-spectrum thioesterase inhibitor, resulted in 80% reduction of the fluorescent signal. This suggests that other mitochondrial depalmitoylating enzymes still need to be identified. Physiological mitochondrial substrates for APT1 are currently unknown. Recently, ABHD10 was identified as a mitochondrial depalmitoylase regulating redox homeostasis through depalmitoylation of peroxiredoxin 5 (Cao et al., 2019). A number of palmitoylated proteins have been identified in mitochondria, but the role of palmitoylation is poorly understood (Corvi et al., 2001; Kostiuk et al., 2008; Shen et al., 2017). In peroxiredoxin 5, methylmalonyl semialdehyde dehydrogenase, and carbamoyl phosphate synthetase, the active site cysteine is palmitoylated, which results in enzyme inhibition. Alternatively, it has been speculated that palmitoylation in mitochondria is important for protein-protein interaction or membrane association. Some of the mitochondrial interactors of PREPL (46/75, 61%) are already identified in palmitome studies (SwissPalm; Blanc et al., 2015). However, potential depalmitoylation by PREPL has not been investigated in this study.

Alternatively, PREPL might function independent of its hydrolytic activity. There is growing evidence that, in some processes, e.g., α-synuclein aggregation (Savolainen et al., 2015) and growth cone morphology (Di Daniel et al., 2009), the peptidase activity of PREP only regulates its physiological function (Männistö and García-Horsman, 2017). In this model, peptide or inhibitor binding leads to conformational changes of PREP, thereby changing its interaction with proteins. The physiological role of PREP results from this interaction with other proteins. This biologically active form can be broken by substrate hydrolysis. Similarly, PREPL is shown to be an effector of AP-1 membrane binding, independent of its catalytic activity (Radhakrishnan et al., 2013). Recently, Santos et al. also revealed that PREPL facilitates α-synuclein aggregation through a non-hydrolytic mechanism similar to that observed for PREP (Santos et al., 2020). The relatively low activity of PREPL toward the ester substrates *in vitro* fits such a model.

In conclusion, this study has unveiled a novel role for the uncharacterized mitochondrial protein $PREPL_L$ in mitochondrial gene expression and respiratory chain function. The impaired mitochondrial function in the *Prepl* KO mice and the altered morphology of mitochondria in a PREPL-deficient patient suggest that mitochondrial dysfunction contributes to the clinical phenotype of CMS22. In addition, we established that PREPL is able to cleave (thio)ester substrates rather than peptides and provided a preliminary structural explanation for this selectivity. This paradigm shift provides new clues toward the identification of potential physiological substrates and comprehension of the compound phenotype of patients with CMS22.

Limitations of the study

There are several limitations to the present study. First, although we found a novel catalytic and cellular function of PREPL, we have not yet identified physiological substrates for PREPL in cytosol or mitochondria. Second, the crystal structure was solved in an open conformation, thereby supporting the hypothesis of an induced-fit mechanism. However, co-crystallization with an inhibitor or substrate would provide additional insights into substrate recognition and hydrolysis. Finally, the article focuses on the mitochondrial function of $PREPL_L$ and does not elaborate on the cytosolic function of $PREPL_S$ in vesicular trafficking.

STAR★METHODS

Detailed methods are provided in the online version of this paper and include the following:

- KEY RESOURCES TABLE
- RESOURCE AVAILABILITY
  - Lead contact
  - Materials availability
  - Data and code availability
- EXPERIMENTAL MODEL AND SUBJECT DETAILS
  - Animal models
  - Cell line
- METHOD DETAILS

SUPPLEMENTAL INFORMATION

Supplemental information can be found online at https://doi.org/10.1016/j.isci.2021.103460.

AUTHOR CONTRIBUTIONS

K.R., M.T.M., B.J.F., Y.M., K.B., and E.H.R. conducted the biochemical experiments. J.S., M.V., A.V.V., and R.V.C. performed and analyzed the mitochondrial complex activity studies. M.J.M., C.A.B., and M.D.P. performed crystallography and analyzed the crystal structure. I.L. performed the MAPPIT analysis, supervised by J.T. N.V.G., K.V., L.A., and K.R. performed the EM analysis. B.F.C. supervised the serine hydrolase inhibitor study. J.W.M.C. and L.R. designed and characterized the mouse model. K.R., B.J.F., L.R., D.J.P., and J.W.M.C. designed the research. K.R. and J.W.C. collected and analyzed the data and wrote the manuscript with input from all co-authors.

DECLARATION OF INTERESTS

The authors declare no competing interests.

SUPPORTING CITATION

The following references appear in the Supplemental Information: Dong et al., 2018.

REFERENCES

Abrami, L., Audagnotto, M., Ho, S., Marcaida, M.J., Mesquita, F.S., Anwar, M.U., Sandoz, P.A., Fonti, G., Pojer, F., Dal Peraro, M., et al. (2021). Palmitoylated acyl protein thioesterase APT2 deforms membranes to extract substrate acyl chains. Nat. Chem. Biol. 17, 438–447. https://doi.org/10.1038/s41589-021-00753-2.

Aertgeerts, K. (2004). Crystal structure of human dipeptidyl peptidase IV in complex with a

decapeptide reveals details on substrate specificity and tetrahedral intermediate formation. Protein Sci. 13, 412–421. https://doi.org/10.1110/ps.03460604.

Baile, M.G., Whited, K., and Claypool, S.M. (2013). Deacylation on the matrix side of the mitochondrial inner membrane regulates cardiolipin remodeling. Mol. Biol. Cell 24, 2008–2020. https://doi.org/10.1091/mbc.E13-03-0121.

Bartholdi, D., Asadollahi, R., Oneda, B., Schmitt-Mechelke, T., Tonella, P., Baumer, A., and Rauch, A. (2013). Further delineation of genotype-phenotype correlation in homozygous 2p21 deletion syndromes: first description of patients without cystinuria. Am. J. Med. Genet. 161A, 1853–1859. https://doi.org/10.1002/ajmg.a.35994.

Bartlam, M., Wang, G., Yang, H., Gao, R., Zhao, X., Xie, G., Cao, S., Feng, Y., and Rao, Z. (2004).

Crystal structure of an acylpeptide hydrolase/esterase from aeropyrum pernix K1. Structure 12, 1481–1488. https://doi.org/10.1016/J.STR.2004.05.019.

Beebe, E.T., Makino, S.I., Markley, J.L., and Fox, B.G. (2014). Automated cell-free protein production methods for structural studies. Methods Mol. Biol. 1140, 117–135. https://doi.org/10.1007/978-1-4939-0354-2_9.

Birch-Machin, M.A., Shepherd, I.M., Watmough, N.J., Sherratt, H.S.A., Bartlett, K., Darley-Usmar, V.M., Milligan, D.W.A., Welch, R.J., Aynsley-Green, A., and Turnbull, D.M. (1989). Fatal lactic acidosis in infancy with a defect of complex III of the respiratory chain. Pediatr. Res. 25, 553–559. https://doi.org/10.1203/00006450-198905000-00025.

Bisogno, T., Howell, F., Williams, G., Minassi, A., Cascio, M.G., Ligresti, A., Matias, I., Schiano-Moriello, A., Paul, P., Williams, E.-J., et al. (2003). Cloning of the first sn1-DAG lipases points to the spatial and temporal regulation of endocannabinoid signaling in the brain. J. Cell Biol. 163, 463–468. https://doi.org/10.1083/jcb.200305129.

Blanc, M., David, F., Abrami, L., Migliozzi, D., Armand, F., Bürgi, J., and van der Goot, F.G. (2015). SwissPalm: protein palmitoylation database. F1000Res. 4, 1–23. https://doi.org/10.12688/f1000research.6464.1.

Bracke, A., Van Elzen, R., Van Der Veken, P., Augustyns, K., De Meester, I., and Lambeir, A.-M. (2019). The development and validation of a combined kinetic fluorometric activity assay for fibroblast activation protein alpha and prolyl oligopeptidase in plasma. Clin. Chim. Acta 495, 154–160. https://doi.org/10.1016/J.CCA.2019.04.063.

Braz, L.P., Ng, Y.S., Gorman, G.S., Schaefer, A.M., McFarland, R., Taylor, R.W., Turnbull, D.M., and Whittaker, R.G. (2019). Neuromuscular junction abnormalities in mitochondrial disease. Neurol. Clin. Pract. 11, 97–104. https://doi.org/10.1212/cpj.0000000000000795.

Butler, M.G., Haber, L., Mernaugh, R., Carlson, M.G., Price, R., and Feurer, I.D. (2001). Decreased bBone mMineral dDensity in Prader-Willi sSyndrome: cComparison wWith oObese Subjects. Am. J. Med. Genet. 103, 216–222. https://doi.org/10.1002/AJMG.1556.

Cámara, Y., Asin-Cayuela, J., Park, C.B., Metodiev, M.D., Shi, Y., Ruzzenente, B., Kukat, C., Habermann, B., Wibom, R., Hultenby, K., et al. (2011). MTERF4 regulates translation by targeting the methyltransferase NSUN4 to the mammalian mitochondrial ribosome. Cell Metab 13, 527–539. https://doi.org/10.1016/j.cmet.2011.04.002.

Canning, P., Rea, D., Morty, R.E., and Fülöp, V. (2013). Crystal structures of Trypanosoma brucei oligopeptidase B broaden the paradigm of catalytic regulation in prolyl oligopeptidase family enzymes. PLoS One 8, e79349. https://doi.org/10.1371/journal.pone.0079349.

Cao, Y., Qiu, T., Kathayat, R.S., Azizi, S.A., Thorne, A.K., Ahn, D., Fukata, Y., Fukata, M., Rice, P.A., and Dickinson, B.C. (2019). ABHD10 is an S-depalmitoylase affecting redox homeostasis through peroxiredoxin-5. Nat. Chem. Biol. 15,

1232–1240. https://doi.org/10.1038/s41589-019-0399-y.

Capozzi, A., Casa, S.D., Altieri, B., and Pontecorvi, A. (2013). Low bone mineral density in a growth hormone deficient (GHD) adolescent. Clin. Cases Miner. Bone Metab. 10, 203–205. https://doi.org/10.11138/ccmbm/2013.10.3.203.

Chabrol, B., Martens, K., Meulemans, S., Cano, A., Jaeken, J., Matthijs, G., and Creemers, J.W.M. (2008). Deletion of C2orf34, PREPL and SLC3A1 causes atypical hypotonia-cystinuria syndrome. J. Med. Genet. 45, 314–318. https://doi.org/10.1136/jmg.2007.055475.

Chaouch, A., Porcelli, V., Cox, D., Edvardson, S., Scarcia, P., De Grassi, A., Pierri, C.L., Cossins, J., Laval, S.H., Griffin, H., et al. (2014). Mutations in the mitochondrial citrate carrier SLC25A1 are associated with impaired neuromuscular transmission. J. Neuromuscul. Dis. 1, 75–90. https://doi.org/10.3233/JND-140021.

Corvi, M.M., Soltys, C.-L.M., and Berthiaume, L.G. (2001). Regulation of mitochondrial carbamoyl-phosphate synthetase 1 activity by active site fatty acylation. J. Biol. Chem. 276, 45704–45712. https://doi.org/10.1074/jbc.M102766200.

Di Daniel, E., Glover, C.P., Grot, E., Chan, M.K., Sanderson, T.H., White, J.H., Ellis, C.L., Gallagher, K.T., Uney, J., Thomas, J., et al. (2009). Prolyl oligopeptidase binds to GAP-43 and functions without its peptidase activity. Mol. Cell. Neurosci. 41, 373–382. https://doi.org/10.1016/j.mcn.2009.03.003.

DiMauro, S., Servidei, S., Zeviani, M., DiRocco, M., DeVivo, D.C., DiDonato, S., Uziel, G., Berry, K., Hoganson, G., Johnsen, S.D., et al. (1987). Cytochrome c oxidase deficiency in leigh syndrome. Ann. Neurol. 22, 498–506. https://doi.org/10.1002/ana.410220409.

Dong, R., Pan, S., Peng, Z., Zhang, Y., and Yang, J. (2018). MTM-align: aA server for fast protein structure database search and multiple protein structure alignment. Nucleic Acids Res. 46, W380–W386. https://doi.org/10.1093/nar/gky430.

Emsley, P., and Cowtan, K. (2004). Coot: model-building tools for molecular graphics. Acta Crystallogr. Sect. D Biol. Crystallogr. 60, 2126–2132. https://doi.org/10.1107/S0907444904019158.

Emsley, P., Lohkamp, B., Scott, W.G., and Cowtan, K. (2010). Features and development of Coot. Acta Crystallogr D Biol Crystallogr 66, 486–501. https://doi.org/10.1107/S0907444910007493.

Filippova, E.V., Weston, L.A., Kuhn, M.L., Geissler, B., Gehring, A.M., Armoush, N., Adkins, C.T., Minasov, G., Dubrovska, I., Shuvalova, L., et al. (2013). Large scale structural rearrangement of a serine hydrolase from francisella tularensis facilitates catalysis. J. Biol. Chem. 288, 10522–10535. https://doi.org/10.1074/jbc.M112.446625.

Fischer, J.C., Ruitenbeek, W., Gabreëls, F.J.M., Janssen, A.J.M., Renier, W.O., Sengers, R.C.A., Stadhouders, A.M., ter Laak, H.J., Trijbels, J.M.F., and Veerkamp, J.H. (1986). A mitochondrial encephalomyopathy: the first case with an established defect at the level of coenzyme Q.

Eur. J. Pediatr. 144, 441–444. https://doi.org/10.1007/BF00441735.

Floyd, B.J., Wilkerson, E.M., Veling, M.T., Minogue, C.E., Xia, C., Beebe, E.T., Wrobel, R.L., Cho, H., Kremer, L.S., Alston, C.L., et al. (2016). Mitochondrial protein interaction mapping identifies regulators of respiratory chain function. Mol. Cell 63, 621–632. https://doi.org/10.1016/j.molcel.2016.06.033.

Fülöp, V., Böcskei, Z., and Polgár, L. (1998). Prolyl oligopeptidase: an unusual β-propeller domain regulates proteolysis. Cell 94, 161–170. https://doi.org/10.1016/S0092-8674(00)81416-6.

Harmat, V., Domokos, K., Menyhárd, D.K., Palló, A., Szeltner, Z., Szamosi, I., Beke-Somfai, T., Náray-Szabó, G., and Polgár, L. (2011). Structure and catalysis of acylaminoacyl peptidase: cClosed and open subunits of a dimer oligopeptidase. J. Biol. Chem. 286, 1987–1998. https://doi.org/10.1074/jbc.M110.169862.

Jaeken, J., Martens, K., Francois, I., Eyskens, F., Lecointre, C., Derua, R., Meulemans, S., Slootstra, J.W., Waelkens, E., de Zegher, F., et al. (2006). Deletion of PREPL, a gene encoding a putative serine oligopeptidase, in patients with hypotonia-cystinuria syndrome. Am. J. Hum. Genet. 78, 38–51. https://doi.org/10.1086/498852.

Janssen, A.J., Trijbels, F.J., Sengers, R.C., Smeitink, J.A., van den Heuvel, L.P., Wintjes, L.T., Stoltenborg-Hogenkamp, B.J., and Rodenburg, R.J. (2007). Spectrophotometric assay for complex I of the respiratory chain in tissue samples and cultured fibroblasts. Clin. Chem. 53, 729–734. https://doi.org/10.1373/clinchem.2006.078873.

Kabsch, W. (2010). XDS. Acta Ccrystallogr. Sect. D Biol. Crystallogr. 66, 125–132. https://doi.org/10.1107/S0907444909047337.

Kanungo, S., Morton, J., Neelakantan, M., Ching, K., Saeedian, J., and Goldstein, A. (2018). Mitochondrial disorders. Ann. Transl. Med. 6, 475. https://doi.org/10.21037/atm.2018.12.13.

Kathayat, R.S., Elvira, P.D., and Dickinson, B.C. (2017). A fluorescent probe for cysteine depalmitoylation reveals dynamic APT signaling. Nat. Chem. Biol. 13, 150–152. https://doi.org/10.1038/nchembio.2262.

Kiss, A.L., Hornung, B., Rádi, K., Gengeliczki, Z., Sztáray, B., Juhász, T., Szeltner, Z., Harmat, V., and Polgár, L. (2007). The acylaminoacyl peptidase from aeropyrum pernix K1 thought to be an exopeptidase displays endopeptidase activity. J. Mol. Biol. 368, 509–520. https://doi.org/10.1016/j.jmb.2007.02.025.

Kostiuk, M.A., Corvi, M.M., Keller, B.O., Plummer, G., Prescher, J.A., Hangauer, M.J., Bertozzi, C.R., Rajaiah, G., Falck, J.R., and Berthiaume, L.G. (2008). Identification of palmitoylated mitochondrial proteins using a bio-orthogonal azido-palmitate analogue. FASEB J. 22, 721–732. https://doi.org/10.1096/fj.07-9199com.

Legati, A., Reyes, A., Nasca, A., Invernizzi, F., Lamantea, E., Tiranti, V., Garavaglia, B., Lamperti, C., Ardissone, A., Moroni, I., et al. (2016). New genes and pathomechanisms in mitochondrial disorders unraveled by NGS technologies. Biochim. Biophys. Acta - Bioenerg. 1857, 1326–

1335. https://doi.org/10.1016/j.bbabio.2016.02.022.

Li, M., Chen, C., Davies, D.R., and Chiu, T.K. (2010). Induced-fit mechanism for prolyl endopeptidase. J. Biol. Chem. *285*, 21487–21495. https://doi.org/10.1074/jbc.M109.092692.

Liebschner, D., Afonine, P.V., Baker, M.L., Bunkoczi, G., Chen, V.B., Croll, T.I., Hintze, B., Hung, L.W., Jain, S., McCoy, A.J., et al. (2019). Macromolecular structure determination using X-rays, neutrons and electrons: recent developments in Phenix. Acta Crystallogr. Sect. D Struct. Biol. *75*, 861–877. https://doi.org/10.1107/S2059798319011471.

Lievens, S., Van der Heyden, J., Masschaele, D., De Ceuninck, L., Petta, I., Gupta, S., De Puysseleyr, V., Vauthier, V., Lemmens, I., De Clercq, D.J.H., et al. (2016). Proteome-scale binary interactomics in human cells. Mol. Cell. Proteomics *15*, 3624–3639. https://doi.org/10.1074/mcp.M116.061994.

Lin, D.T.S., and Conibear, E. (2015). ABHD17 proteins are novel protein depalmitoylases that regulate N-Ras palmitate turnover and subcellular localization. Elife *4*, e11306. https://doi.org/10.7554/eLife.11306.

Liu, Y., Patricelli, M.P., and Cravatt, B.F. (1999). Activity-based protein profiling: the serine hydrolases. Proc. Natl. Acad. Sci. *96*, 14694–14699. https://doi.org/10.1073/pnas.96.26.14694.

Livak, K.J., and Schmittgen, T.D. (2001). Analysis of relative gene expression data using real-time quantitative PCR and the 2−ΔΔCT method. Methods *25*, 402–408. https://doi.org/10.1006/meth.2001.1262.

Lone, A.M., Bachovchin, D.A., Westwood, D., Speers, A.E., Timothy, P., Fernandez-vega, V., Chase, P., Hodder, P.S., Rosen, H., Cravatt, B.F., et al. (2012). A substrate-free activity-based protein profiling screen for the discovery of selective PREPL inhibitors. J. Am. Chem. Soc. *133*, 11665–11674. https://doi.org/10.1021/ja2036095.A.

Lone, A.M., Leidl, M., McFedries, A.K., Horner, J.W., Creemers, J., and Saghatelian, A. (2014). Deletion of PREPl causes growth impairment and hypotonia in mice. PLoS One *9*, e89160. https://doi.org/10.1371/journal.pone.0089160.

Männistö, P.T., and García-Horsman, J.A. (2017). Mechanism of action of Prolyl oligopeptidase (PREP) in degenerative brain diseases: hHas peptidase activity only a modulatory role on the interactions of PREP with proteins? Front. Aging Neurosci. *9*, 1–10. https://doi.org/10.3389/fnagi.2017.00027.

Markley, J.L., Aceti, D.J., Bingman, C.A., Fox, B.G., Frederick, R.O., Makino, S.I., Nichols, K.W., Phillips, G.N., Primm, J.G., Sahu, S.C., et al. (2009). The center for eukaryotic structural genomics. J. Struct. Funct. Genomics. *10*, 165–179. https://doi.org/10.1007/s10969-008-9057-4.

Martens, K., Derua, R., Meulemans, S., Waelkens, E., Jaeken, J., Matthijs, G., and Creemers, J.W.M. (2006). PREPL: a putative novel oligopeptidase propelled into the limelight. Biol. Chem. *387*, 879–883. https://doi.org/10.1515/BC.2006.111.

Martens, K., Heulens, I., Meulemans, S., Zaffanello, M., Tilstra, D., Hes, F.J., Rooman, R., François, I., de Zegher, F., Jaeken, J., et al. (2007). Global distribution of the most prevalent deletions causing hypotonia–cystinuria syndrome. Eur. J. Hum. Genet. *15*, 1029–1033. https://doi.org/10.1038/sj.ejhg.5201881.

Martin, B.R., Wang, C., Adibekian, A., Tully, S.E., and Cravatt, B.F. (2012). Global Pprofiling of Ddynamic Pprotein Ppalmitoylation. Nat. Methods *9*, 84–89. https://doi.org/10.1038/nmeth.1769.

Mayr, J.A., Haack, T.B., Freisinger, P., Karall, D., Makowski, C., Koch, J., Feichtinger, R.G., Zimmermann, F.A., Rolinski, B., Ahting, U., et al. (2015). Spectrum of combined respiratory chain defects. J. Inherit. Metab. Dis. *38*, 629–640. https://doi.org/10.1007/s10545-015-9831-y.

McCoy, A.J., Grosse-Kunstleve, R.W., Adams, P.D., Winn, M.D., Storoni, L.C., and Read, R.J. (2007). Phaser crystallographic software. J. Appl. Crystallogr. *40*, 658–674. https://doi.org/10.1107/S0021889807021206.

Meulemans, A., Seneca, S., Lagae, L., Lissens, W., De Paepe, B., Smet, J., Van Coster, R., and De Meirleir, L. (2006). A novel mitochondrial transfer RNAAsn mutation causing multiorgan failure. Arch. Neurol. *63*, 1194–1198. https://doi.org/10.1001/archneur.63.8.1194.

Morawski, M., Nuytens, K., Juhasz, T., Zeitschel, U., Seeger, G., Waelkens, E., Regal, L., Schulz, I., Arendt, T., Szeltner, Z., et al. (2013). Cellular and ultra structural evidence for cytoskeletal localization of prolyl endopeptidase-like protein in neurons. Neuroscience *242*, 128–139. https://doi.org/10.1016/j.neuroscience.2013.02.038.

Nunnari, J., and Suomalainen, A. (2012). Mitochondria: iln sickness and in health. Cell *148*, 1145–1159. https://doi.org/10.1016/j.cell.2012.02.035.

ORFeome Collaboration (2016). The ORFeome collaboration: a genome-scale human ORF-clone resource. Nat. Methods *13*, 191–192. https://doi.org/10.1038/nmeth.3776.

Pagliarini, D.J., Calvo, S.E., Chang, B., Sheth, S.A., Vafai, S.B., Ong, S.E., Walford, G.A., Sugiana, C., Boneh, A., Chen, W.K., et al. (2008). A mitochondrial protein compendium elucidates complex I disease biology. Cell *134*, 112–123. https://doi.org/10.1016/j.cell.2008.06.016.

Pánek, T., Eliáš, M., Vancová, M., Lukeš, J., and Hashimi, H. (2020). Returning to the fold for lessons in mitochondrial crista diversity and evolution. Curr. Biol. *30*, R575–R588. https://doi.org/10.1016/j.cub.2020.02.053.

Parvari, R., Brodyansky, I., Elpeleg, O., Moses, S., Landau, D., and Hershkovitz, E. (2001). A recessive contiguous gene deletion of chromosome 2p16 associated with cystinuria and a mitochondrial disease. Am. J. Hum. Genet. *69*, 869–875. https://doi.org/10.1086/323624.

Poveda-Huertes, D., Mulica, P., and Vögtle, F.N. (2017). The versatility of the mitochondrial presequence processing machinery: cleavage, quality control and turnover. Cell Tissue Res *367* (1), 73–81. https://doi.org/10.1007/s00441-016-2492-9.

Quinn, D.M. (1987). Acetylcholinesterase: enzyme structure, reaction dynamics, and virtual transition states. Chem. Rev. *87*, 955–979. https://doi.org/10.1021/cr00081a005.

Radhakrishnan, K., Baltes, J., Creemers, J.W.M., and Schu, P. (2013). Trans-Golgi network morphology and sorting is regulated by prolyl-oligopeptidase-like protein PREPL and the AP-1 complex subunit μ1A. J. Cell Sci. *126*, 1155–1163. https://doi.org/10.1242/jcs.116079.

Randhawa, R., and Cohen, P. (2005). The role of the insulin-like growth factor system in prenatal growth. Mol. Genet. Metab. *86* (1-2), 84–90. https://doi.org/10.1016/j.ymgme.2005.07.028.

Raudvere, U., Kolberg, L., Kuzmin, I., Arak, T., Adler, P., Peterson, H., and Vilo, J. (2019). g:Profiler: a web server for functional enrichment analysis and conversions of gene lists (2019 update). Nucleic Acids Res. *47*, W191–W198. https://doi.org/10.1093/nar/gkz369.

Régal, L., Mårtensson, E., Maystadt, I., Voermans, N., Lederer, D., Burlina, A., Juan Fita, M.J., Hoogeboom, A.J.M., Olsson Engman, M., Hollemans, T., et al. (2018). PREPL deficiency: delineation of the phenotype and development of a functional blood assay. Genet. Med. *20*, 109–118. https://doi.org/10.1038/gim.2017.74.

Régal, L., Shen, X.-M., Selcen, D., Verhille, C., Meulemans, S., Creemers, J.W.M., and Engel, A.G. (2014). PREPL deficiency with or without cystinuria causes a novel myasthenic syndrome. Neurology *82*, 1254–1260. https://doi.org/10.1212/WNL.0000000000000295.

Rhee, H.-W., Zou, P., Udeshi, N.D., Martell, J.D., Mootha, V.K., Carr, S.A., and Ting, A.Y. (2013). Proteomic mapping of mitochondria in living cells via spatially restricted enzymatic tagging. Science *339*, 1328–1331. https://doi.org/10.1126/science.1230593.

Richter, U., Lahtinen, T., Marttinen, P., Myöhänen, M., Greco, D., Cannino, G., Jacobs, H.T., Lietzén, N., Nyman, T.A., and Battersby, B.J. (2013). A mitochondrial ribosomal and RNA decay pathway blocks cell proliferation. Curr. Biol. *23*, 535–541. https://doi.org/10.1016/j.cub.2013.02.019.

Robert, X., and Gouet, P. (2014). Deciphering key features in protein structures with the new ENDscript server. Nucleic Acids Res. *42*, W320–W324. https://doi.org/10.1093/nar/gku316.

Rustin, P., Chretien, D., Bourgeron, T., Gérard, B., Rötig, A., Saudubray, J.M., and Munnich, A. (1994). Biochemical and molecular investigations in respiratory chain deficiencies. Clin. Chim. Acta *228*, 35–51. https://doi.org/10.1016/0009-8981(94)90055-8.

Santos, G.S., Oyadomari, W.Y., Carvalho, E.A., Torquato, R.S., and Oliveira, V. (2020). Prolyl endopeptidase-like facilitates the α-synuclein aggregation seeding, and this effect is reverted by serine peptidase inhibitor PMSF. Biomolecules *10*, 962. https://doi.org/10.3390/biom10060962.

Savolainen, M.H., Yan, X., Myöhänen, T.T., and Huttunen, H.J. (2015). Prolyl oligopeptidase enhances α-Synuclein dimerization via direct protein-protein interaction. J. Biol. Chem. *290*,

5117–5126. https://doi.org/10.1074/jbc.M114. 592931.

Schneider, C.A., Rasband, W.S., and Eliceiri, K.W. (2012). NIH Image to ImageJ: 25 years of image analysis. Nat. Methods 9, 671–675. https://doi.org/10.1038/nmeth.2089.

Scholte, H.R., Ross, J.D., Blom, W., Boonman, A.M.C., van Diggelen, O.P., Hall, C.L., Huijmans, J.G.M., Luyt-Houwen, I.E.M., Kleijer, W.J., de Klerk, J.B.C., et al. (1992). Assessment of deficiencies of fatty acyl-CoA dehydrogenases in fibroblasts, muscle and liver. J. Inherit. Metab. Dis. 15, 347–352. https://doi.org/10.1007/BF02435973.

Shan, L., Mathews, I., and Khosla, C. (2005). Structural and mechanistic analysis of two prolyl endopeptidases: role of interdomain dynamics in catalysis and specificity. PNAS 102, 3599–3604. https://doi.org/10.1073/pnas.0408286102.

Shayman, J.A., and Tesmer, J.J.G. (2019). Lysosomal phospholipase A2. Biochim. Biophys. Acta - Mol. Cell Biol. Lipids 1864, 932–940. https://doi.org/10.1016/j.bbalip.2018.07.012.

Shen, L.-F., Chen, Y.-J., Liu, K.-M., Haddad, A.N.S., Song, I.-W., Roan, H.-Y., Chen, L.-Y., Yen, J.J.Y., Chen, Y.-J., Wu, J.-Y., et al. (2017). Role of S-palmitoylation by ZDHHC13 in mitochondrial function and metabolism in liver. Sci. Rep. 7, 2182. https://doi.org/10.1038/s41598-017-02159-4.

Simon, G.M., and Cravatt, B.F. (2010). Activity-based proteomics of enzyme superfamilies: serine hydrolases as a case study. J. Biol. Chem. 285, 11051–11055. https://doi.org/10.1074/jbc.R109.097600.

Smet, J., Seneca, S., De Paepe, B., Meulemans, A., Verhelst, H., Leroy, J., De Meirleir, L., Lissens, W., and Van Coster, R. (2009). Subcomplexes of mitochondrial complex V reveal mutations in mitochondrial DNA. Electrophoresis 30, 3565–3572. https://doi.org/10.1002/elps.200900213.

Sottocasa, G.L., Kuylenstierna, B., Ernster, L., and Bergstrand, A. (1967). An electron-transport system associated with the outer membrane of liver mitochondria. J. Cell Biol. 32, 415–438. https://doi.org/10.1083/jcb.32.2.415.

Stafforini, D.M., McIntyre, T.M., Carter, M.E., and Prescott, S.M. (1987). Human plasma platelet-activating factor acetylhydrolase. Association with lipoprotein particles and role in the degradation of platelet-activating factor. J. Biol. Chem. 262, 4215–4222. https://doi.org/10.1016/S0021-9258(18)61335-3.

Stark, C., Breitkreutz, B.J., Reguly, T., Boucher, L., Breitkreutz, A., and Tyers, M. (2006). BioGRID: a general repository for interaction datasets. Nucleic Acids Res. 34, 535–539. https://doi.org/10.1093/nar/gkj109.

Szczepanowska, K., Maiti, P., Kukat, A., Hofsetz, E., Nolte, H., Senft, K., Becker, C., Ruzzenente, B., Hornig-Do, H., Wibom, R., et al. (2016). CLPP coordinates mitoribosomal assembly through the regulation of ERAL1 levels. EMBO J. 35, 2566–2583. https://doi.org/10.15252/embj.201694253.

Szeltner, Z., Alshafee, I., Juhász, T., Parvari, R., and Polgár, L. (2005). The PREPL A protein, a new member of the prolyl oligopeptidase family, lacking catalytic activity. Cell. Mol. Life Sci. 62, 2376–2381. https://doi.org/10.1007/s00018-005-5262-5.

Tsirigotaki, A., Van Elzen, R., Van Der Veken, P., Lambeir, A.-M., and Economou, A. (2017). Dynamics and ligand-induced conformational changes in human prolyl oligopeptidase analyzed by hydrogen/deuterium exchange mass spectrometry. Sci. Rep. 7, 2456. https://doi.org/10.1038/s41598-017-02550-1.

Van Coster, R., Smet, J., George, E., De Meirleir, L., Seneca, S., Van Hove, J., Sebire, G., Verhelst, H., De Bleecker, J., Van Vlem, B., et al. (2001). Blue native polyacrylamide gel electrophoresis: a powerful tool in diagnosis of oxidative

phosphorylation defects. Pediatr. Res. 50, 658–665. https://doi.org/10.1203/00006450-200111000-00020.

Wang, Q., Yang, G., Liu, Y., and Feng, Y. (2006). Discrimination of esterase and peptidase activities of acylaminoacyl peptidase from hyperthermophilic Aeropyrum pernix K1 by a single mutation. J. Biol. Chem. 281, 18618–18625. https://doi.org/10.1074/jbc.M601015200.

Wortmann, S.B., Koolen, D.A., Smeitink, J.A., van den Heuvel, L., and Rodenburg, R.J. (2015). Whole exome sequencing of suspected mitochondrial patients in clinical practice. J. Inherit. Metab. Dis. 38, 437–443. https://doi.org/10.1007/s10545-015-9823-y.

Yang, J., Roy, A., and Zhang, Y. (2013). Protein-ligand binding site recognition using complementary binding-specific substructure comparison and sequence profile alignment. Bioinformatics 29, 2588–2595. https://doi.org/10.1093/bioinformatics/btt447.

Yang, X., Boehm, J.S., Yang, X., Salehi-Ashtiani, K., Hao, T., Shen, Y., Lubonja, R., Thomas, S.R., Alkan, O., and Bhimdi, T. (2011). A public genome-scale lentiviral expression library of human ORFs. Nat. Methods 8, 659–661. https://doi.org/10.1038/nmeth.1638.

Yang, J., Yan, R., Roy, A., Xu, D., Poisson, J., and Zhang, Y. (2014). The I-TASSER suite: protein structure and function prediction. Nat. Methods. 12, 7–8. https://doi.org/10.1038/nmeth.3213.

Ye, C., Shen, Z., and Greenberg, M.L. (2016). Cardiolipin remodeling: a regulatory hub for modulating cardiolipin metabolism and function. J. Bioenerg. Biomembr. 48, 113–123. https://doi.org/10.1007/s10863-014-9591-7.

Zeidman, R., Jackson, C.S., and Magee, A.I. (2009). Protein acyl thioesterases (Review). Mol. Membr. Biol. 26, 32–41. https://doi.org/10.1080/09687680802629329.

STAR★METHODS

KEY RESOURCES TABLE

REAGENT or RESOURCE	SOURCE	IDENTIFIER
Antibodies		
Mouse monoclonal anti-human PREPL (E-9)	Santa Cruz Biotechnology	Cat# sc-393321
Alexa 488-conjugated rabbit anti-mouse antibody	Life technologies	Cat# A11059; RRID:AB_142495
Monoclonal anti-FLAG M2 antibody	Sigma	Cat# F1804; RRID:AB_262044
Alexa 594-conjugated goat anti-mouse antibody	Life technologies	Cat#A32742; RRID:AB_2762825
Mouse polyclonal anti-human PREPL MaxPab (B01P)	Abnova	Cat# H00009581-B01P; RRID:AB_1711714
Mouse monoclonal β-actin (8H10D10) antibody	Cell signaling technology	Cat#3700S; RRID:AB_2242334
Rabbit monoclonal MT-Cytochrome B	ABclonal Technology	Cat# A9762; RRID:AB_2770455
Rabbit polyclonal COX4 antibody	Cell signaling technology	Cat# 4844; RRID:AB_208542
Mouse monoclonal VDAC1 antibody (B-6)	Santa Cruz Biotechnology	Cat# sc-390996; RRID:AB_2750920
Mouse monoclonal GST (B-14) antibody	Santa Cruz Biotechnology	Cat# sc-138; RRID:AB_627677
Streptavidin-HRP	Agilent	P039701
Polyclonal rabbit anti-mouse/HRP	Agilent	P0260
Polyclonal Swine anti-rabbit/HRP	Agilent	P0217
Bacterial and virus strains		
pGEX-2T Rosetta (DE3)pLysS	Novagen	71403
Chemicals, peptides, and recombinant proteins		
MitoTracker™ Red CMX Ros	Thermo Fischer Scientific	M7512
FP-biotin	Santa Cruz Biotechnology	sc-215056
Heparin	Leo Pharma NV, Belgium	NA
Beta-nicotinamide adenine dinucleotide (NADH)	Merck	N8129
Rotenone	Merck	R8875
KCN	Merck	60178
Decylubiquinone	Merck	D7911
DCPIP	Merck	D1878
Antimycin A	Merck	A8674
Sodium succinate	Merck	S2378
Malonate	Merck	M1875
Cytochrome C	Merck	C7752
NaBH4	Merck	71320
Sodium hydrosulfite	Merck	71699
Acetyl CoA	Merck	A2056
DTNB	Merck	D8130
Oxaloacetic acid	Merck	O4126
Aminocaproic acid	Merck	A7824
n-Dodecyl β-D-maltoside (laurylmaltoside)	Merck	D4641
Serva blue G	Serva	35050
Nitrotetrazolium blue chloride (NBT)	Merck	N6876
Phenazine methosulfate (PMS)	Merck	P9625
Sodium succinate dibasic hexahydrate	Merck	S2378
1-Step™ TMB-Blotting substrate solution	Thermo Fischer Scientific	34018
3,3′-diaminobenzidine (DAB)	Merck	D8001

(Continued on next page)

Continued

REAGENT or RESOURCE	SOURCE	IDENTIFIER
Catalase from bovine liver	Merck	C9322
Lead(II)nitrate	Merc	228621
Adenosine 5′-triphosphate disodium salt hydrate	Merck	A2383
Inhibitors for competitive ABPP (Table S4)	Dr. Ben Cravatt	NA
Inhibitor 8	Vitas-M technology	STK649251
Palmostatin B	Merck	178501
p-nitrophenyl thioacetate (NPTA)	Sigma	S888524
p-nitrophenyl acetate (pNP2)	Sigma	N8130
p-nitrophenyl butyrate (pNP4)	Sigma	N9876
p-nitrophenyl octanoate (pNP8)	Sigma	21742
p-nitrophenyl decanoate (pNP10)	Sigma	N0252
p-nitrophenyl dodecanoate (pNP12)	Sigma	61716
p-nitrophenyl myristate (pNP14)	Sigma	70124
p-nitrophenyl palmitate (pNP16)	Sigma	N2752
z-Gly-Pro-AMC	Bachem	4002518
z-Arg-Arg-AMC	Bachem	4004789
Recombinant human His-PREP	Dr. Anne-Marie Lambeir	NA
KYP-2047	Dr. Anne-Marie Lambeir	NA
Recombinant human APT1	Sanbio	TP760001
Dolethal	Vetoquinol	NA
Critical commercial assays		
Mitochondrial isolation kit for cultured cells	Thermo Fischer Scientific	89874
Pierce™ Coomassie (Bradford) protein assay kit	Thermo Fischer Scientific	23200
Pierce™ Modified Lowry assay	Thermo Fischer Scientific	2340
Luciferase assay system	Promega	E1500
Thrombin cleavage capture kit	Novagen	69,022
Deposited data		
Human PREPL$_S$ crystal structure	This paper	PDB: 7OBM
Experimental models: Cell lines		
Human: HEK293T cells	ATCC	CRL-3216
Experimental models: Organisms/strains		
Mouse: PREPL-ex10(Fl) tm Lox KO	This paper	NA
Mouse: PREPL-ex10(Fl) tm Lox KO (BL6)	This paper	NA
Oligonucleotides		
Primers for mouse genotyping, see Table S6	This paper	NA
Primers for MAPPIT cloning, see Table S6	This paper	NA
Primers for RT-qPCR, see Table S6	This paper	NA
Recombinant DNA		
pcDNA3.1-FLAG-human PREPL (WT, G652E)	This paper	NA
pcDNA3.1-FLAG-E.coli OpdB (WT, E624G)	This paper	NA
8His-[TEV]-hPREPLs (residues 90-727)	This paper	NA
pSEL(+2L)	Dr. Jan Tavernier	NA
pCLG20	Dr. Jan Tavernier	NA
pMG1	Dr. Jan Tavernier	NA

Continued

REAGENT or RESOURCE	SOURCE	IDENTIFIER
pXP2d2-rPAP1-luciferase reporter	Dr. Jan Tavernier	NA
pSEL(+2L)-PREPL	This paper	NA
pCLG20-PREPL	This paper	NA
Software and algorithms		
ImageJ	Schneider et al. (2012)	https://imagej.nih.gov/im/
BioRender	–	www.biorender.com
PyMOL	PyMOL Molecular Graphics System, Schrödinger, LLC	https://pymol.org
XDS	Kabsch (2010)	https://xds.mr.mpg.de
Phenix	Liebschner et al. (2019)	https://www.phenix-online.org
PHASER	McCoy et al. (2007)	www-structmed.cimr.cam.ac.uk/phaser_obsolete
iTASSER	Yang et al., 2014	http://zhanglab.dcmb.med.umich.edu/I-TASSER
Coot	Emsley et al., 2010	www2.mrc-lmb.cam.ac.uk/personal/pemsley/coot/
ESPript	Robert and Gouet, 2014	https://espript.ibcp.fr
COACH	Yang et al. (2013)	http://zhanglab.ccmb.med.umich.edu/COACH/
Other		

RESOURCE AVAILABILITY

Lead contact

Further information and requests for resources and reagents should be directed to and will be fulfilled by the lead contact, John WM Creemers (john.creemers@kuleuven.be).

Materials availability

Prepl KO mice generated in this study are available from the Lead contact with a completed Materials Transfer Agreement.

Data and code availability

- X-ray diffraction data and PDB coordinates were deposited in the Protein DataBank and will be released on 10 November 2021. The entry is entitled 'Crystal structure of the human Prolyl Endopeptidase-Like protein short form (residues 90-727)'. The accession number is listed in the key resources table.

- This paper does not report original code.

- Any additional information required to reanalyze the data reported in this paper is available from the lead contact upon request.

EXPERIMENTAL MODEL AND SUBJECT DETAILS

Animal models

Generation and genotyping of Prepl KO mouse.   A 10.8 kb fragment containing exon 8 to exon 12 of murine *Prepl* from a C57BL/6 BAC clone was used to construct the targeting vector. The hygromycin B selection cassette was introduced in the intron downstream of exon 10. The cassette was flanked by Frt sites for later excision by Flp recombinase. Exon 10 and the hygromycin B selection cassette were flanked by 2 *LoxP* sites. The region was subcloned into pGEM-T Easy (Promega) in antisense orientation, downstream of the EcoRI and SalI site. The targeting construct was linearized by SalI and electroporated in embryonic stem cells (ES). After selection with hygromycin B, surviving clones were expanded for Southern blot and PCR analysis to identify recombinant ES clones. Mice were generated in collaboration with Ingenious Targeting Laboratory, Inc. (Stony Brook, NY, USA). Targeted ES were microinjected into C57BL/6 blastocysts. Chimeras were mated to WT C57BL/6 homozygous Flp mice to remove the Hygromycin B cassette and generate heterozygous F1 mice. To obtain *in vivo* inactivation of the floxed *Prepl* allele, F1 mice were mated with PGK-Cre general deleter mice. Heterozygous mice were backcrossed with C57BL/6 mice to create the 1x backcrossed mice (50% C57BL/6N/25%129S6/25%SW; official nomenclature of the strain:

Prepl-ex10(Fl) tm Lox KO). These mice were intercrossed to obtain *Prepl* WT, heterozygous or KO mice. In parallel, the 1x backcrossed mice were backcrossed with C57BL/6 mice for 8 generations to obtain heterozygous mice with a >99% C57BL/6 background (official nomenclature of the strain: Prepl-ex10(Fl) tm Lox KO BL6). Genotyping was carried out on ear genomic DNA in 2 PCR reactions. In the Δ PCR a 596 bp or 150 bp DNA fragment was amplified depending on the presence or absence of exon 10. The *LoxP* PCR was performed with primers located up- and downstream of the *LoxP* site downstream of exon 10, resulting in a 179 bp PCR fragment. No PCR fragment is present if recombination occurred. Primers for mouse genotyping are listed in Table S6.

The mice were housed under SPF conditions in standard cages on a 12-h day/night cycle and fed a standard rodent chow. All animal experiments were approved by the ethical research committee of KU Leuven in accordance with the declaration of Helsinki (KU Leuven project number (282/2015)).

DEXA measurements.   Body composition of 1x backcrossed mice was assessed by DEXA scan using the Lunar Piximus (GE healthcare). Mice were anesthetized before scanning and were placed with their stomach down. ROI was adapted not to include the head. During the anesthesia, the mice were measured from the tip of the nose to the base of the tail.

Cell line
HEK293T cells (ATCC) were grown in DMEM (Thermo Fischer Scientific) supplemented with 10% FCS (VWR). Cells were maintained at ~75% confluency at 37°C with 5% CO_2.

METHOD DETAILS
General techniques
Plasmids and transfection.   HEK293T cells were transfected with pcDNA3.1 containing cDNAs encoding WT or variants of PREPL and OpdB using the Xtreme Gene 9 transfection reagent (Sigma Aldrich) according to the manufacturer's protocol. Point mutations were introduced by PCR-based mutagenesis and confirmed by direct sequencing.

Immunoprecipitation and cell fractionation.   24 h post-transfection, cells were lysed in PBS by passaging through a 26-gauge needle. After removal of the cell debris, FLAG-tagged proteins were immunopurified for 2 h at 4°C using preformed complexes of anti-FLAG M2 antibody (Sigma Aldrich) and protein G Sepharose (GE healthcare). After incubation, the beads were washed three times with ice-cold PBS and used for activity assay and Western blot analysis as described later. Mitochondrial and cytosolic fractions from HEK293T cells were obtained using the Mitochondria Isolation Kit for cultured cells (Thermo Fisher Scientific) according to the manufacturer's protocol.

Western blot.   Protein concentrations were determined using the Pierce BCA Protein assay kit (Thermo Fisher Scientific). Proteins were denatured, separated by SDS-PAGE and transferred to a nitrocellulose membrane. Membranes were blocked with 5% nonfat dry milk in PBS with 0.2% Triton X-100. Membranes were labeled overnight with primary antibody at 4°C. Subsequently, the blot was incubated with horseradish peroxidase-conjugated secondary antibodies (Dako) and proteins were detected with the Western Lightning ECL System (Perkin Elmer). Images were quantified using ImageJ software (Schneider et al., 2012).

Mitochondrial function
MAPPIT.   A pcDNA3.1-FLAG-PREPL plasmid, containing full-length human PREPL$_S$ (NP_001165088.1) and an amino-terminal fused FLAG-tag, was used as a template for cloning PREPL in the bait vectors pSEL(+2L) and pCLG20. The PCR product contained full-length PREPL flanked by a SalI and NotI restriction site for cloning in the pSEL(+2L) vector and full-length PREPL flanked by a SacI and ApaI restriction site for cloning in the pCLG20 plasmid, hereby creating the bait constructs used for the MAPPIT screen. The primers used for cloning the bait constructs are listed in Table S6. PREPL insertion was confirmed by direct sequencing. The bait constructs were screened against the human ORFeome v8.1 (Yang et al., 2011) and ORFeome Collaboration (ORFeome Collaboration, 2016) prey library in the pMG1 vector (14817 constructs). MAPPIT was in collaboration with Dr. Irma Lemmens (Ghent University, Belgium). HEK293T cells were seeded in a 96 well (10,000 cells/well). Cells were transfected with 250 ng bait, 500 ng prey and 50 ng pXP2d2-rPAP1-luciferase reporter plasmids using the CaPO4 transient transfection method. 24 h

post-transfection cells were stimulated with 100 ng/mL leptin (pCLG20 construct) or 5 ng/mL Epo (pSEL(+2-L construct) in DMEM. The following day, the luciferase activity was measured using the Luciferase Assay System kit (Promega) on an Envision luminometer (Perkin Elmer). Each specific bait-prey interaction was studied in parallel with two controls (irrelevant bait (IB; pSEL(+2L) or pCLG20) and irrelevant prey (IP; pMG1)). The fold change of the specific bait-prey interaction (stimulated/non-stimulated) should be at least 3 times higher than the fold change of the control samples (Lievens et al., 2016).

Immunofluorescence confocal microscopy. To study localization of endogenous PREPL, HEK293T cells, grown on coverslips, were stained with 250 nM Mitotracker Red CMX Ros (Thermo Fisher Scientific) in DMEM supplemented with 10% FCS for 30 min at 37°C. Subsequently, the cells were fixed with 4% formaldehyde and 4% sucrose in PBS for 30 min at room temperature and permeabilized with PBS supplemented with 0.2% Triton X-100 for 10 min at room temperature. After blocking for 1 h at 4°C with PBS containing 2% FCS, 2% BSA, 0.2% gelatin and 5% rabbit serum (Gentaur), cells were incubated with a mouse monoclonal antibody raised against human PREPL (1:50; sc393321, Santacruz) for 1 h at room temperature. Alexa 488-conjugated rabbit anti-mouse antibody (1:2500; A11059; Life technologies) was used as secondary antibody. The coverslips were then mounted with Vectashield containing DAPI (Vector laboratories). Cells were analyzed with a Nikon C2 Eclipse Ni-E confocal microscope.

On the day prior to transfection, HEK293T cells were plated at a density of 75,000 cells/well onto poly-D-lysine-coated coverslips in 6-well dishes. Cells were transiently co-transfected with pcDNA3.1-PREPL-FLAG and a plasmid encoding GFP with an amino-terminal mitochondrial targeting sequence (MTS-GFP). After 24 h, the cells were fixed with 4% formaldehyde in PBS, permeabilized with 0.2% Triton X-100 in PBS, blocked with 1% BSA in PBS, and probed with mouse anti-FLAG M2 antibody (1:2000; F1804; Sigma) and Alexa Fluor 594-conjugated goat anti-mouse antibody (1:2000; A32742; Life technologies) in 1% BSA in PBS. Hoechst dye was used to label nuclear DNA. Slides were placed in mounting medium (1:1 glycerol:PBS). Confocal images were captured using the Nikon A1R system, Plan Apo VC 60X oil immersion optics, with sequential laser excitation using 561 nm (Alexa Fluor), 488 nm (GFP), and 408 nm (Hoechst) lasers. Images were collected and assembled into a Z-stack using the NIS Elements software.

Mitochondrial complex activity assay and BN-PAGE. Mice were sacrificed by cervical dislocation and tissues were snap frozen in liquid nitrogen and stored at −80°C. Female mice were kept for breeding purposes. In collaboration with Dr. Rudy Van Coster (Ghent University Hospital, Ghent University), spectrophotometric assays were performed to measure the activity of the mitochondrial complexes in mouse quadriceps, cortex and cerebellum. To prepare tissue homogenate of post-nuclear homogenates, 50 mg of tissue was excised, transferred to a tube on ice containing 19 volumes of ice cold buffer (10μM Tris-HCl, 0.25 M sucrose, 2 mM EDTA and 50 U/ml heparin, pH 7.4) and minced using scissors. The tissues were homogenized using a motor driven glass/glass pestle by applying 20 strokes at 800 rpm. In case of brain tissue, the mixture was sonicated using a probe sonicator for 2 s at medium intensity. The resulting homogenates were centrifuged at 5600 g for 1 min for skeletal muscle and 2 min for brain tissue (Scholte et al., 1992). The pellets consisting of cell debris were discarded and the supernatants containing the mitochondria were kept at −80°C until spectrophotometric evaluation of OXPHOS activities and measurement of protein content was performed using the Pierce™ Modified Lowry Assay kit (Thermo Fisher Scientific, cat. 2340) according to the manufacturer instructions. To summarize, whole tissue homogenate was prepared and protein content was measured using the Lowry method. Complex I activity in brain samples was measured by incubating the tissue homogenates in 25 mM potassium phosphate buffer (pH 7.5), 2.5 mg/mL BSA, 5 mM $MgCl_2$, 100 μM NADH and 0.6 mM KCN. After homogenization and stabilization for 1 min at 37°C, decylubiquinone (130 μM final) was added. The NADH oxidation was determined at 340 nm for 3 min (Fischer et al., 1986). For muscle, the tissue homogenates were incubated in 25 mM phosphate buffer (pH 7.8), 5 mM BSA, 0.6 mM DCPIP, 7 mM decylubiquinone, 0.1 mM antimycin. After homogenization and stabilization for 3 min at 37°C, NADH (10 mM) was added and DCPIP reduction was determined at 600 nm for 4 min. Inhibition with 1μM of rotenone was performed immediately after to determine the rotenone-insensitive fraction (Janssen et al., 2007). Complex II activity measurements were performed by incubation of the tissue homogenates in 10 mM potassium phosphate buffer (pH 7.5), 20 mM sodium succinate and 3 mM KCN (Rustin et al., 1994). After homogenization and stabilization for 5 min. at 37°C, DCPIP (50μM final) and decylubiquinone (130μM final) were added. DCPIP reduction was determined at 600 nm for 4 min. Inhibition with 5 mM malonate was performed in parallel to determine the malonate-insensitive fraction. For complex III, a mix of 900 μL complex III buffer (31 mM KH_2PO_4, 3 mM EDTA, 0.6 mM KCN and 27.5 mM DMSO; pH 7.5), 10μL decylubiquinole (produced by reducing decylubiquinone with $NaBH_4$) and 100μL

cytochrome c (1% in 10 mM potassium phosphate buffer pH 7.0) was prepared. After homogenization and stabilization for 3 min at 37°C, tissue homogenates were added and reduction of cytochrome c was detected at 550 nm for 4 min. Inhibition with 1μM antimycin A was performed in parallel to determine the antimycin-insensitive fraction (Birch-Machin et al., 1989). Complex IV activity was measured by preparing a mix of potassium phosphate buffer pH 7.0 (10 mM final) and 0.1% cytochrome c (1% in 10 mM potassium phosphate buffer pH 7.0) reduced with sodium hydrosulfite in water. After homogenization and stabilization for 10 min at 37°C, tissue homogenates were added and oxidation of cytochrome c was monitored at 550 nm for 4 min (DiMauro et al., 1987). Finally, for combined complex II+III activity, the tissue homogenates were incubated in 10 mM potassium phosphate buffer (pH 7.5), 20 mM sodium succinate and 3 mM KCN. After homogenization and stabilization for 2 min at 37°C, cytochrome C (oxidized form) (0.1 % final) was added. Reduction of cytochrome c was detected at 550 nm for 4 min (Sottocasa et al., 1967). The enzymatic activity of each complex was normalized relative to citrate synthase activity. This was measured by incubating the tissue homogenates in 0.1 mM Tris-HCl buffer (pH 8.1), 60 μM AcCoA, 100 μM DTNB and 0.05% Triton X-100. After stirring and stabilization for 2 min at 37°C, oxaloacetic acid (0.5 mM final) was added. Reaction with DTNB was detected at 412 nm for 4 min (Meulemans et al., 2006).

BN-PAGE and in-gel activity staining.   Mitochondria were isolated from 100 mg of tissue as described for the complex activity measurements. The supernatant containing the mitochondria was kept on ice and the pellet was resuspended with 19 volumes of buffer and treated two times as described above. The combined supernatants were centrifuged for 4 min at 37,500 g. After washing the pellet, the pellet was resuspended in 1.9 mL and homogenized manually by applying 10 strokes with a glass-glass pestle. Following centrifugation at 5600 g for 30 s, the resulting supernatant was centrifuged at 16,100 g for 15 min. For BN-PAGE analysis, the mitochondrial pellets are re-suspended in 120–150 μL of 750 mM aminocaproic acid, 50 mM Bis-Tris/HCl (pH 7.0) and 1.1% laurylmaltoside. After centrifugation at 16,100 g for 15 min, the supernatant containing the oxidative phosphorylation enzyme complexes was kept on ice. Protein amount of the solubilized mitochondrial proteins was measured with the Pierce™ Coomassie (Bradford) Protein Assay Kit (Thermo Fisher Scientific cat. 23200). Prior to loading on the Blue Native gel, 5% Serva Blue G and 750 mM aminocaproic acid is added to 100 μL of solubilized proteins and vortexed. Samples are loaded in duplicate. Electrophoresis is first performed with the colored cathodal buffer (50 mM Tris and 15 mM Bis-Tris and 0.02% Serva Blue G) and anodal (25 mM Bis-Tris) buffer, both at 4°C for 1.5 h at 80V, until the front reaches the resolving gel. The colored cathodal buffer is then replaced with the non-coloured cathodal buffer (50 mM Tris and 15 mM Bis-Tris) and run at 200V at 4°C, until the Serva Blue tracking dye runs off the gel (for 2-3 h). When separation is terminated, gels are stored at −80°C until further evaluation using in-gel activity staining. Complex I activity was evaluated after incubation with 2 mM Tris-HCl 0.3 mM NADH, 3.5 mM NBT (pH 7.4) at 37°C for 3-4 h. Complex II activity was evaluated after incubation in a medium containing 4.5 mM EDTA, 10 mM KCN, 0.2 mM phenazine methosulfate, 84 mM sodium succinate and 10 mM Nitro Blue tetrazolium chloride in 1.5 mM phosphate buffer (pH 7.4) at 37°C for 3-4 h. Complex III staining was obtained by incubation with the 1-Step™ TMB-Blotting Substrate Solution (Thermo Fisher Scientific) at 37°C, bands reach maximum intensity after 5-6 h. Complex IV staining was achieved after incubation in 50 mM phosphate buffer (pH 7.4), containing 2.3 mM 3,3'-diaminobenzidine, 2 μg/mL catalase, 1 mg/mL cytochrome c and 220 mM sucrose (pH 7.4) at 37°C. Bands reach maximum intensity after 5-6 h. Complex V activity was evaluated by incubating the gels in 35 mM Tris, 270 mM glycine, 14 mM MgSO$_4$, 0.2% Pb(NO$_3$)$_2$, and 8 mM ATP (pH 7.8) at 37°C, bands reach maximum intensity after 3-4 h. Gel fragments are scanned using an Epson Perfection V800 Photo Scanner with Silverfast software, both in reflection modus (complex V) and in transmission modus (complex I-IV) (Van Coster et al., 2001).

Scanning electron microscopy of quadriceps.   Mice were anesthetized by an intraperitoneal injection with Dolethal (Vetoquinol) and transcardially perfused with 4% formaldehyde, 2.5% glutaraldehyde and 0.2% picric acid in 0.1 M sodium cacodylate buffer (pH 7.2). Quadriceps were removed, longitudinal sections of 1 mm x 1 mm x 3 mm were cut and dissolved in fresh fixative for O/N incubation at 4°C. Samples were post-fixed in 1% osmium tetroxide and 1.5% potassium ferrocyanide in 0.1 M sodium cacodylate buffer for 1 h. Counterstaining was obtained by incubating the sections in 0.5% uranyl acetate. After washing, samples were incubated *en bloc* with lead aspartate (0.02 M lead nitrate in 0.03 M sodium aspartate, pH 5.5), followed by washing with MilliQ and dehydration with increasing concentrations of ethanol. Sections were then embedded in epoxy resin. 200 μm sections of 1 mm x 3 mm were cut on a Leica ultracut S microtome and collected on indium-tin-oxide coverslips. After mounting the coverslips on 25 mm diameter stubs with carbon tabs and silverpaint, sections were imaged on a Zeiss Sigma Variable Pressure Scanning Electron Microscope. Only slow-twitch muscle fibers containing high concentrations of mitochondria were imaged.

RT-qPCR of complex subunits. RNA isolation from mice quadriceps was performed using the RNeasy Fibrous Tissue Mini kit (Qiagen). cDNA was synthesized with the iScript cDNA synthesis kit (BioRad). Real-time PCR was performed in triplicate with the CFX Connect™ Real-Time PCR Detection system (Bio-Rad) using SsoAdvanced™ Universal SYBR® Green Supermix (BioRad). Data were analyzed using the Livak method (Livak and Schmittgen, 2001). Primers used for RT-qPCR are listed in Table S6.

Enzymatic activity

Bacterial expression of PREPL. Human WT and inactive serine mutant PREPLs cDNA were cloned in-frame with GST in pGEX-2T. Rosetta (DE3)pLysS (Novagen) were transformed with the plasmids and grown overnight. A single colony was used to inoculate a 50 mL LB culture containing 100 μg/μL ampicillin and 25 μg/μL chloramphenicol and grown overnight at 37°C. A 50 mL starter culture was prepared with 1 mL of overnight culture. When OD_{600} reached about 0.5, two 400 mL cultures were inoculated with 10 mL of the starter culture. At OD_{600} = 0.6, IPTG was added to a final concentration of 0.1 mM and the culture was incubated overnight at 26°C. Cells were harvested by centrifugation and frozen at −20°C for 1 hour to help cell lysis. The pellets were thawed by resuspension in PBS (pH 7.4) containing 2 mM EDTA and 2 mM DTT. Cells were sonicated for 20 min (10 sec on, 20 sec off). After centrifugation at 3,500 rpm at 4°C for 30 min, Triton X-100 was added to a final concentration of 1% in order to keep the GST-tagged protein soluble. The supernatant was cleared by centrifugation at 13,000 rpm at 4°C for 30 min and filtration through a 0.22 micron filter. Glutathione sepharose 4B resin (GE Healthcare), pre-equilibrated with PBS, was added to the cleared supernatant and incubated for at least 30 min. GST tagged proteins were eluted in 50 mM Tris-HCl containing 10 mM reduced glutathione (pH 8). Samples were subjected to SDS-PAGE and the gel was stained using GelCode™ Blue stain reagent (Thermo Fisher Scientific). The concentration was determined using bovine serum albumin as a standard.

Competitive ABPP and FP-biotin assay. Competition experiments were performed in 50 mM phosphate buffer (pH 8) supplemented with 10 mM EDTA and 2 mM DTT. 75 nM bacterially expressed PREPL or immunopurified PREPL was pre-incubated with 10 μM inhibitor or DMSO (0.05% final concentration) as a control at 37°C for 15 min. This was followed by a reaction with 1.5 μM FP-biotin (Santa Cruz Biotechnology, sc-215056) at 37°C for 15 min. The reaction was stopped with the addition of SDS-PAGE loading buffer and denaturing the sample at 95°C for 10 min. Western blot analysis using a Streptavidin-HRP antibody (Agilent) was performed to evaluate the potential inhibition of PREPL. Membranes were stripped and relabeled with the GST antibody (Santa Cruz Biotechnology; sc138) to detect the presence of PREPL. Serine hydrolase inhibitors were kindly provided by Dr. Ben Cravatt (Scripps Research Institute, USA). Palmostatin B was purchased from Merck (cat. 178501). 1-isobutyl-3-oxo-3,5,6,7-tetrahydro-2H-cyclopenta[c]pyridine-4-carbonitrile was purchased from Vitas-M Laboratory (STK649251).

AMC substrate assay PREP. Human recombinant His-tagged PREP and KYP-2047 (UAMC-714) were kindly provided by Dr. Anne-Marie Lambeir (University of Antwerp, Belgium). Purified PREP was incubated with DMSO or a serine hydrolase inhibitor for 15 min at 37°C. Subsequently, 200 μM of z-Gly-Pro-AMC (Bachem), a fluorogenic substrate of PREP, was added. The reaction was performed in 50 mM phosphate buffer (pH 8) supplemented with 1 mM DTT. Fluorescence was measured with a FLUOstar Galaxy microplate reader (BMG Labtech) at excitation and emission wavelengths of 390 and 460 nm respectively.

AMC substrate assay OpdB. After immunoprecipitation, the beads containing FLAG-tagged OpdB were separated in a 2:1 ratio for AMC assay:WB analysis. The AMC assay was performed by incubating the beads in 50 mM phosphate buffer (pH8) supplemented with 10 mM EDTA and 2 mM DTT. After 30 minutes incubation at 37°C, 200 μM z-Arg-Arg-AMC (Bachem) was added. Fluorogenic leaving groups were detected as described for PREP. Western blot was performed for normalization purposes. The beads were resuspended in 1x sample buffer containing 1% β mercaptoethanol. After 10 min at 95°C, the samples were analyzed by western blotting.

(Thio)esterase activity assay. The GST-tag of bacterially expressed PREPL was removed using the Thrombin Cleavage capture kit (Novagen) to avoid hydrolysis of the p-nitrophenyl esters by GST. Uncleaved GST-PREPL and excess of biotin-linked thrombin was removed by immunoprecipitation with Streptavidin beads (Thermo Fisher Scientific) and Glutathione sepharose 4B beads (GE Healthcare). The activity of the GST-cleaved PREPL was evaluated in an activity assay with FP-biotin. The esterase activity assay was performed in reaction buffer (50 mM Tris pH 7.4, 150 mM NaCl, 0.5% Triton X-100) with 0.5 mM of various

p-nitrophenyl ester substrates. Stocks of ester substrates were prepared in acetonitrile. The reaction was started by the addition of 0.5 μM bacterially expressed WT or inactive serine mutant PREPL. The released product p-nitrophenol was measured by monitoring the absorbance at 405 nm for 30 min with a Victor X3 plate reader (Perkin Elmer). Thioesterase activity was assessed with 0.05 mM p-nitrophenyl thioacetate (NPTA) in 60 mM MOPS reaction buffer (pH 7.5) containing 0.2 M KCl and 0.5 μM of WT or mutant PREPL. Product formation was measured spectrophotometrically at 405 nm. The kinetic parameters k_{cat}, K_m and V_{max} were determined with the substrate concentration range of 0-2 mM for pNP2 and pNP4 and 0-200 μM for NPTA. Data analysis was performed with a non-linear regression of the Michaelis-Menten equation using GraphPad Prism (GraphPad Software, USA). pNP substrates were purchased from Sigma. Recombinant APT1 was obtained from Sanbio (TP760001).

Structure of PREPL$_S$

Expression and purification. 8His-[TEV]-hPREPLs (residues 90-727) was evaluated for expression in both *E. coli* and wheat germ cell free platforms of the Mitochondrial Proteome Partnership (Markley et al., 2009). Selenomethionyl protein was expressed and purified by wheat-germ cell-free expression (Beebe et al., 2014). Protein was expressed in a 16 mL scale in a Protemist 100 production run. The protein was purified by IMAC chromatography using a 1 mL HisTrap column, 50 mM Tris (pH 7.8), 300 mM NaCl, 2 mM DTT, 50-500 mM imidazole gradient. The captured protein was concentrated and buffer exchanged into 10 mM HEPES (pH 7), 100 mM NaCl, 0.6 mM TCEP prior to TEV cleavage (1:10 molar ratio of TEV protease, 17 hours at 293K). The reaction products were purified by subtractive IMAC, purified by gel filtration on a S200 column in the same buffer, and concentrated with buffer exchange to 20.1 mg/mL in 5 mM HEPES, pH 8.0, 50 mM NaCl, 0.3 mM TCEP.

Crystallization of human PREPL$_S$. Crystals were prepared by the sitting-drop vapor diffusion method. 200 nL of protein and 200 nL of reservoir (Hampton IndexHT) were combined in an MRC SD2 crystallization plate using a Mosquito crystallization robot. Crystals were discovered after 1 year equilibration against a reservoir solution consisted of 2 M ammonium sulfate and 0.1 M Na-HEPES buffer (pH 7.5) at 277K.

Data collection and structure refinement. Crystals were cryopreserved by briefly soaking in reservoir solution overlain with Fomblin-Y and supplemented with 30% sucrose. Crystals were flash cooled by direct immersion in liquid nitrogen. A diffraction data set was collected at the Se-peak wavelength (0.979420 Å) to 3.1 Å resolution at beamline 23-ID-B, at the Advanced Photon Source. The data were processed with XDS (Kabsch, 2010). Crystals belonged to the space group I222 with cell dimensions a = 64.92 Å, b = 150.88 Å, c = 220 Å. Matthews calculations predicted the asymmetric unit of the crystal to contain one molecule, with a solvent content of ~66.5%. The structure was solved by a combination of Se-SAD phasing in Phenix (Liebschner et al., 2019) and molecular replacement with PHASER (McCoy et al., 2007). Homology models build by iTASSER (Yang et al., 2014) were used as search models. The positions of the Se-Met atoms were corroborated by anomalous Fourier from the calculated phases from the molecular replacement model and used as guideposts in building. Refinement was performed with Phenix. Iterative cycles of model building with Coot (Emsley and Cowtan, 2004) and restrained refinement were performed. The final model contains one molecule in the asymmetric unit with almost all residues (except 101-107 and 720-727 that could not be modeled) and no Ramachandran outliers. Statistics from data processing and model refinement are shown in Table S5. Figures were prepared using PyMOL (The PyMOL Molecular Graphics System, Schrödinger, LLC.) and ESPript (Robert and Gouet, 2014). Coordinate and structure factors were deposited in the Protein Data Bank (PDB accession code 7OBM). Ligand docking was performed using the COACH server (Yang et al., 2013).

QUANTIFICATION AND STATISTICAL ANALYSIS

All statistical analyses were performed with GraphPad Prism 8 or 9. Statistical analysis was performed by unpaired two-sided Student's t-tests for two groups and one-way ANOVA with Dunnett's multiple comparison for more than two groups. Comparison of observed proportions of KO mice with theoretically expected proportions was done with the binomial test. Data are represented as mean $\pm$ SEM. Significance shown on graphs as $*p < 0.05$, $**p < 0.01$ or $***p < 0.001$. Statistical details can be found in the figure legends.